Received: 30 May 2023 | Revised: 14 September 2023 | Accepted: 18 September 2023

DOI: 10.1002/jev2.12369

RESEARCH ARTICLE

Engineering a tunable micropattern-array assay to sort single extracellular vesicles and particles to detect RNA and protein in situ

Jingjing Zhang[1] | **Xilal Y. Rima**[1] | **Xinyu Wang**[1] | **Luong T. H. Nguyen**[1] | **Kristin Huntoon**[2,3] | **Yifan Ma**[1] | **Paola Loreto Palacio**[4] | **Kim Truc Nguyen**[1] | **Karunya Albert**[1] | **Minh-Dao Duong-Thi**[1] | **Nicole Walters**[1] | **Kwang Joo Kwak**[5] | **Min Jin Yoon**[1] | **Hong Li**[1] | **Jacob Doon-Ralls**[1] | **Colin L. Hisey**[1] | **Daeyong Lee**[2] | **Yifan Wang**[6] | **Jonghoon Ha**[6] | **Kelsey Scherler**[7] | **Shannon Fallen**[7] | **Inyoul Lee**[7] | **Andre F. Palmer**[1] | **Wen Jiang**[6] | **Setty M. Magaña**[4] | **Kai Wang**[7] | **Betty Y. S. Kim**[2,3] | **L. James Lee**[1,5] | **Eduardo Reátegui**[1,8]

[1]William G. Lowrie Department of Chemical and Biomolecular Engineering, The Ohio State University, Columbus, Ohio, USA

[2]Department of Neurosurgery, The University of Texas MD Anderson Cancer Center, Houston, Texas, USA

[3]The Brain Tumor Center, The University of Texas MD Anderson Cancer Center, Houston, Texas, USA

[4]Department of Pediatrics, Division of Neurology, Nationwide Children's Hospital, Columbus, Ohio, USA

[5]Spot Biosystems Ltd., Palo Alto, California, USA

[6]Department of Radiation Oncology, The University of Texas Southwestern Medical Center, Dallas, Texas, USA

[7]Institute for Systems Biology, Seattle, Washington, USA

[8]Comprehensive Cancer Center, The Ohio State University, Columbus, Ohio, USA

Correspondence
Eduardo Reátegui, William G. Lowrie Department of Chemical and Biomolecular Engineering, The Ohio State University, Columbus, OH 43210, USA.
Email: reategui.8@osu.edu

Funding information
National Institutes of Health; National Center for Advancing Translational Sciences, Grant/Award Numbers: U18TR003807, UG3TR002884, UH3TR002884

Abstract

The molecular heterogeneity of extracellular vesicles (EVs) and the co-isolation of physically similar particles, such as lipoproteins (LPs), confounds and limits the sensitivity of EV bulk biomarker characterization. Herein, we present a single-EV and particle (siEVP) protein and RNA assay (^{siEVP}PRA) to simultaneously detect mRNAs, miRNAs, and proteins in subpopulations of EVs and LPs. The ^{siEVP}PRA immobilizes and sorts particles via positive immunoselection onto micropatterns and focuses biomolecular signals in situ. By detecting EVPs at a single-particle resolution, the ^{siEVP}PRA outperformed the sensitivities of bulk-analysis benchmark assays for RNA and protein. To assess the specificity of RNA detection in complex biofluids, EVs from various glioma cell lines were processed with small RNA sequencing, whereby two mRNAs and two miRNAs associated with glioblastoma multiforme (GBM) were chosen for cross-validation. Despite the presence of single-EV-LP co-isolates in serum, the ^{siEVP}PRA detected GBM-associated vesicular RNA profiles in GBM patient siEVPs. The ^{siEVP}PRA effectively examines intravesicular, intervesicular, and interparticle heterogeneity with diagnostic promise.

Jingjing Zhang, Xilal Y. Rima and Xinyu Wang contributed equally to this work.

KEYWORDS
extracellular RNA, glioblastoma multiforme, heterogeneity, multiparametric, single extracellular vesicle, single lipoprotein

1 | INTRODUCTION

Extracellular vesicles (EVs) are small membranous vesicles secreted by cells that are trafficked intercellularly and present in various biofluids (Yáñez-Mó et al., 2015). EVs are involved in various biological processes from immunomodulation to embryonic development (Kalluri & LeBleu, 2020). In cancer, EVs promote drug resistance (Santos et al., 2018; Zeng et al., 2017), immunosuppression (Filipazzi et al., 2012; Yekula et al., 2020), the epithelial-to-mesenchymal transition (Chen et al., 2017; Conigliaro & Cicchini, 2018), disruption of the blood-brain barrier (Tominaga et al., 2015), and organotropism (Hoshino et al., 2015; Rodrigues et al., 2019). However, the biomolecular composition of EVs is highly heterogeneous, with proteins, RNAs, DNAs, lipids, and metabolites reflecting their tissue of origin (Gatto et al., 2021; Westphal & Lamszus, 2015). Despite the potential use of EVs in the clinic for diagnostics, current methods for isolating and characterizing EVs are technically challenging (Mateescu et al., 2017; Momen-Heravi et al., 2013; Ramirez et al., 2018), partly due to the co-isolation of physically similar particles present in complex biofluids, such as lipoproteins (LPs) (Brennan et al., 2020; Tian et al., 2019; Yuana et al., 2014). As such, isolation methods are cumbersome and irreproducible, yielding isolation-dependent vesicular profiles (Koster et al., 2021; Royo et al., 2016; Van Deun et al., 2014). On the other hand, conventional characterization methods, such as western blot (WB), enzyme-linked immunosorbent assay (ELISA), quantitative reverse-transcriptase polymerase chain reaction (qRT-PCR), next-generation sequencing (NGS), and mass spectroscopy (MS) require vesicular lysis to obtain intraluminal contents. Emerging evidence on the complexity of single EV and particle (siEVP) co-isolates in complex biofluids and cell culture media (Busatto et al., 2020, 2022; Sódar et al., 2016; Tóth et al., 2021; Wolf et al., 2022), suggests that the lysis of EVPs convolutes the interparticle complexity of biofluids and mutes their inherent heterogeneity. Therefore, there is an unmet need to develop technologies that provide an accurate and efficient analysis of the biomolecular content in siEVPs without compromising the structural integrity of the particles.

Several analytical methods are frequently employed to quantify the physical and biomolecular characteristics of intact single EVs (siEVs), including optical and non-optical techniques (Hilton & White, 2021; Kwon & Park, 2022; Qiu et al., 2023). Nanoparticle tracking analysis (NTA), tunable resistive pulse sensing (TRPS), and microfluidic resistive pulse sensing (MRPS) are routinely used to measure the size and concentration of siEVs, with the minimum detectable size in the 50–100 nm range (Arab et al., 2021; Thane et al., 2019; van der Pol et al., 2014; Vogel et al., 2021). However, NTA, TRPS, and MRPS integrate siEVP signals non-specifically due to limitations in phenotyping (Panagopoulou et al., 2020). Atomic force microscopy (AFM), scanning electron microscopy (SEM), and transmission electron microscopy (TEM) are often utilized to provide morphological and mechanical properties of siEVs while surpassing the optical limit of diffraction (Noble et al., 2020; Pascucci & Scattini, 2021; Ridolfi et al., 2020; Yurtsever et al., 2021). Although some distinguishing characteristics amongst the siEVPs are present, physically similar siEVPs are often undiscernible, and results are user-dependent (Karttunen et al., 2018; Piontek & Roos, 2022; Rikkert et al., 2019; Zhang et al., 2011). Incorporating immunogold labeling with TEM can provide additional phenotyping of siEVP surface proteins, but the technique is low throughput, labor intensive, and rarely quantitative (Erdbrügger & Lannigan, 2016). Accordingly, nanoflow cytometry (nFCM), which can detect siEVPs as small as 40 nm, based on the intensity of side-scattered photons, can identify subpopulations of siEVs via surface protein composition by incorporating fluorescently labeled antibodies (Tian et al., 2019). However, reduced multiplexed capability, inability to detect low-expressing biomarkers, particle swarming due to required concentrations, and extensive calibration requirements have limited their use (Kwon & Park, 2022; Salmond et al., 2021). Optical techniques can also be applied to tunable signal-enhancing surfaces, such as plasmonic and interferometric surfaces, to examine siEV surface protein composition via immunoselective immobilization (Daaboul et al., 2016; Yang et al., 2018). Furthermore, antibody-DNA conjugates incorporating random-tag sequences in a proximity barcoding assay with NGS have been used to improve the simultaneous profiling of surface proteins in siEVs (Wu et al., 2019). Although these promising technologies have demonstrated their ability to resolve subpopulations of siEVs from different tissues, the complex intraluminal cargo of siEVs, such as nucleic acids, still requires the same rigor and optimization. On the other hand, evidence on the bioactivity of LP-transported miRNA (Vickers et al., 2011) and LP-bound proteins (Mackness et al., 1991) has inspired novel engineering approaches for their quantification (Kumar et al., 2023; Zhang et al., 2022). However, to our knowledge, in situ biomarker quantification has not been performed at a single LP (siLP) resolution.

Recently, super-resolution microscopy has been applied to detect and quantify fluorescent signals at the sub-vesicular level affording unprecedented detection limits to aid in interpreting siEV heterogeneity (Panagopoulou et al., 2020). Direct stochastic optical reconstruction microscopy (dSTORM) has been utilized to spatially locate the presence of proteins on siEVs and reconstruct siEVs in three dimensions (McNamara et al., 2022). Furthermore, super-resolution microscopy has advanced towards visualizing siEVs in complex biofluids, such as quantitative single-molecule localization microscopy (qSMLM), which detected

the protein content of siEVs from plasma (Lennon et al., 2019; Saftics et al., 2023), as well as total internal reflection fluorescence microscopy (TIRFM), which detected protein, miRNA, and mRNA in siEVs in plasma and serum utilizing liposomal fusion (Hu et al., 2017; Nguyen et al., 2022; Wu et al., 2013; Zhou et al., 2020). However, using liposomes alters the native structure of siEVs and can lead to higher background signals due to electrostatic interactions with the liposomes (Hu et al., 2017; Nguyen et al., 2022; Wu et al., 2013; Zhou et al., 2020). Although the immobilization strategies utilized may insufficiently sort out non-EV particles and co-isolates (Bonté & Juliano, 1986; Busatto et al., 2020, 2022; Sódar et al., 2016), most of these diagnostic investigations omit the possible interaction of similar blood-derived particles. Therefore, a facile assay to multiplex protein and RNA in siEVPs from complex biofluids without altering their native structure while also considering interactions with siLPs is needed.

Herein we describe the siEVP protein and RNA assay (^{siEVP}PRA), capable of multiplexing protein and RNA biomarker detection at a single-particle resolution. The assay consists of an array of micropatterns surrounded by a non-biofouling polymer film that can be functionalized with various antibodies to sort and immobilize siEVPs. In this investigation, we targeted ADP-ribosylation factor 6 (ARF6), annexin A1, CD63, and CD9 as EV-specific epitopes; epidermal growth factor receptor (EGFR) as a tumor-specific epitope; and apolipoprotein A1 (ApoA1) and apolipoprotein B (ApoB) as LP-specific epitopes to immobilize and quantify siEVP subpopulations, revealing intervesicular and interparticle heterogeneity. RNA-targeting molecular beacons (MBs) and fluorescently labeled antibodies generated signals for mRNA, miRNA, and protein on siEVPs, which were then visualized by TIRFM and quantified via automatic image acquisition. By focusing signals via in situ detection at a single-particle resolution, the ^{siEVP}PRA exceeded the detection limit for both qRT-PCR and ELISA by three orders of magnitude without tedious lysis and amplification steps. With the enhanced sensitivity of siEVP analyses, we discovered single-LP-EV (siLP-EV) co-isolates expressing CD63 by subjecting serum-isolated siLPs to CD63/CD9-mediated capture on the ^{siEVP}PRA, which were obscured by bulk-analysis methods. Furthermore, the combinatorial multiplexing of various biomarkers across biomolecular species in siEVs allowed us to investigate siEV intravesicular heterogeneity. We validated the RNA detection of intact siEVPs in complex biofluids by performing small RNA sequencing (sRNA-seq) on EVs harvested from six glioma cell lines to identify glioblastoma multiforme (GBM)-associated RNA and extending the ^{siEVP}PRA to profile siEVPs isolated from the serum of GBM patients. This is the first assay that enables the simultaneous and low-dose profiling of protein, miRNA, and mRNA on siEVPs without altering their native structure, lending unique applications for liquid biopsies and biomolecular discovery.

2 | MATERIALS AND METHODS

2.1 | Materials

0.01% (w/v) poly-L-lysine (PLL; MilliporeSigma, Burlington, MA), 5 kDa mPEG-SVA (ThermoFisher Scientific, Waltham, MA), 0.1 M 4-(2-hydroxyethyl)-1-piperazineethanesulfonic acid (HEPES) buffer (pH = 8.50; ThermoFisher Scientific), 4-benzoylbenzyl-trimethylammonium chloride (PLPP; Alvéole, France), NeutrAvidin (NA; ThermoFisher Scientific), bovine serum albumin (BSA; MilliporeSigma), tris-ethylenediaminetetraacetic acid (TE) buffer (pH = 8.05; ThermoFisher Scientific), *E. coli* (VB200815-1011zys), *E. coli* (VB200815-1012qpx), *E. coli* (VB200815-1013ugb) (VectorBuilder Inc., Chicago, IL). Capture and detection antibodies used in the study are provided in Table S1. Capture antibodies (except the select few pre-biotinylated) were biotinylated using an EZ-Link™ micro Sulfo-NHS-biotinylation kit (ThermoFisher Scientific). All MBs used in the study are provided in Table S2.

2.2 | Substrate fabrication

Coverslips were cleaned with ethanol and then deionized (DI) water via sonication for 3 min. The surface of the coverslip was treated with oxygen plasma for 1 min to activate the surface. A small drop of 0.01% (w/v) PLL was placed onto parafilm on which the treated coverslip was then placed for an even distribution of the PLL. After incubating the coverslip for 30 min at room temperature, the PLL-coated coverslip was rinsed with DI water and dried with nitrogen flow. Following the same method, 100 mg/mL of mPEG-SVA diluted in 0.1 M HEPES was evenly distributed on the PLL-coated coverslip. The coverslip was incubated at room temperature for 1 h before rinsing with DI water and drying with a nitrogen airflow.

2.3 | Device fabrication and surface modification

The passivated coverslip was photoetched using the PRIMO optical module (Alvéole) mounted on an automated inverted microscope (Nikon Eclipse Ti Inverted Microscope System, Melville, NY). Briefly, grayscale images were translated into UV light via a digital-micromirror device (DMD) that allows for a maskless illumination of different UV intensities correlating to

the corresponding grayscale values (Strale et al., 2016). Following the passivation of the coverslip, PLPP was diluted in 96% ethanol to distribute the gel evenly throughout the surface of the coverslip. After the ethanol evaporated, a silicone spacer (W × L, 3.5 mm × 3.5 mm, 64 wells; Grace Bio Labs, Bend, OR) was placed on the PEG-coated coverslip. A five-by-five array of 20-μm diameter circles spaced 80 μm center-to-center was exposed onto the coverslip with the PRIMO optical module. To optimize the relative fluorescence intensities (RFIs) between samples and their controls, micropatterns at different grayscale values, including 0, 25, 50, 75, 95 and 100% with UV doses, including 10, 20 and 30 mJ/mm^2 were examined (Table S3). After the UV illumination, the photoetched coverslip was washed under a stream of DI water and dried by nitrogen flow. A microscopy slide (ThermoFisher Scientific) was placed under the coverslip, and the 64-well ProPlate microarray system (Grace Bio Labs) was placed gently on the photoetched coverslip. The assembled array was secured by delrin snap clips (Grace Bio Labs) to avoid leakage or potential contamination. The photoetched coverslip was rehydrated in phosphate-buffered saline (PBS) for 15 min before further functionalizing the micropatterns.

2.4 | Cell culture

U251 and Gli36 glioma cell lines were cultured in Dulbecco's Modified Eagle Medium (DMEM). SF268, SF295, SF539, SNB19, and SNB75 glioma cell lines were cultured in Roswell Park Memorial Institute (RPMI) 1640 medium. All cell culture media was prepared with 10% (v/v) fetal bovine serum (FBS) and 1% (v/v) penicillin-streptomycin. Cell lines were cultured to 70% confluence at 37°C in a 5% CO_2 incubator. Before EV collection, cells were washed with PBS three times, after which the cells were incubated in serum-free media. After two days of cell culture, the EV-enriched cell culture media was collected and centrifuged at 2000 × *g* for 10 min at room temperature to separate cell debris before further analysis.

2.5 | Human tumor specimen collection

GBM patient serum was obtained under Institutional Review Board (IRB)-approved protocols at MD Anderson Cancer Center (PA 19-0661) following national guidelines. All patients signed informed consent forms during clinical visits before surgery and sample collection. Patients did not receive compensation in return for their participation in this study.

2.6 | Healthy donor serum and plasma collection

About 10 mL of whole blood from healthy donors was collected into BD Serum Separation Tubes (SST; ThermoFisher Scientific) and BD Plasma Preparation Tubes (PPT; ThermoFisher Scientific) for serum and plasma collection, respectively. SSTs were gently placed upright to coagulate for 60 min after being rocked 10 times. PPTs were rocked 10 times. Both SSTs and PPTs were centrifuged at room temperature at 1,100 × *g* for 10 min. After centrifugation, the serum and plasma were stored in 1 mL aliquots at −80°C. All blood samples were collected under an approved IRB at The Ohio State University (IRB #2018H0268).

2.7 | LP isolation

Healthy donor serum was subjected to the low-density LP/very-low-density LP (LDL/VLDL) and high-density LP (HDL) purification kits (Cell Biolabs, San Diego, CA). About 1 mL of serum on ice, a dextran solution, and precipitation solution A was added and incubated on ice for 5 min. The sample was centrifuged at 6,000 × *g* for 10 min at 4°C. The supernatant was removed for further HDL processing, while the remaining pellet was subjected to further LDL purification. For LDL purification, the pellet was resuspended in 40 μL of a bicarbonate solution and centrifuged at 6,000 × *g* for 10 min at 4°C, whereby the supernatant was transferred to 1 mL of 1× precipitation solution B and centrifuged at 6,000 × *g* for 10 min at 4°C. The pellet was resuspended with 20 μL of a NaCl solution, added to 1 mL of 1× precipitation solution C, and centrifuged at 6,000 x *g* for 10 min at 4°C. The last process was repeated and after centrifugation, the pellet was resuspended in 20 μL of a NaCl solution. For HDL isolation, the supernatant was added to 60 μL of a dextran solution and 150 μL of precipitation solution A and was then incubated for 2 h at room temperature and centrifuged at 16,000 × *g* for 30 min at 4°C. The pellet was resuspended in 500 μL of an HDL resuspension buffer and centrifuged at 6,000 × *g* for 10 min at 4°C. The pellet was resuspended in 600 μL of a 1× HDL wash solution, incubated on a rocker for 30 min at 4°C, and centrifuged at 6,000 × *g* for 10 min at 4°C. The HDL supernatant was transferred to 90 μL of a dextran removal solution, while the LDL resuspension was added to 80 μL of the dextran removal solution. The mixtures were incubated for 1 h at 4°C and centrifuged at 6,000 × *g* for 10 min at 4°C by which the supernatants were recovered into a 20-kDa Slide-A-Lyzer® MINI Dialysis devices (ThermoFisher Scientific) and incubated in PBS for 1 day.

2.8 | Engineered-EV RNA model system

Cell transfection was conducted via a cellular nanoporation (CNP) biochip (Yang et al., 2020). Briefly, a single layer of Gli36 cells ($\sim 8 \times 10^6$) was spread overnight on a 1 cm × 1 cm 3D CNP silicon chip surface. Individual CNP chips were transfected separately with cel-miR-39-3p, cel-miR-54-3p and cel-miR-238-3p plasmids at 400 ng/μL concentration in PBS. For multi-plasmid transfection, a weight ratio of 1:1:1 was pre-mixed at a 400 ng/μL concentration each in PBS. The plasmid solutions were injected into the cells via nanochannels using a 150 V electric field for 10 pulses, at 10 ms durations and 0.1 s intervals. EVs were collected from the cell supernatant 24 h after cell transfection.

2.9 | Tangential flow filtration (TFF) EVP purification

The EV-enriched cell culture media and serum samples were introduced into a TFF system as described by our previous technique to purify EVPs (Zhang et al., 2021). In brief, cell culture media or serum was circulated through a 500 kDa TFF hollow fiber filter cartridge, where EVPs were retained and enriched in the system (~5 mL), while free proteins and nucleic acids permeated through the filter. Constant-volume diacycles of PBS were performed until pure EVPs were obtained (350 mL of PBS). The EVPs were further enriched by centrifuging the sample within a 10 kDa centrifugal unit at 3,000 × *g* at 4°C until a final volume of 100 μL was achieved. Protein concentrations were measured using a Micro BCA™ Protein Assay kit (ThermoFisher Scientific), according to the manufacturer's protocol.

2.10 | Apolipoprotein corona

EVs with apolipoprotein corona were prepared according to an established protocol (Tóth et al., 2021). Briefly, plasma was diluted into PBS 1:1 and passed through a 2-μm filter then a 0.8-μm filter. The filtered plasma was ultracentrifuged at 20,000 × *g* at 16°C for 40 min. The supernatant was collected and was ultracentrifuged at 100,000 × *g* at 4°C for 16 hr. The supernatant was collected and referred to hereafter as EV-depleted plasma (EVDP). About 60 μL of TFF-purified EVs harvested from Gli36 cells grown in serum-free conditions were incubated in 500 μL of EVDP for 30 min at room temperature. After the incubation, the solution was purified via size-exclusion chromatography (SEC) with the qEV (Izon Sciences, Boston, MA), according to the manufacturer's protocol. The samples were concentrated to 10^9 particles/mL with a 3 kDa centrifugal unit at 3,000 × *g* at 4°C. The purified EVs with apolipoprotein corona were immediately added to the ^{siEVP}PRA.

2.11 | Tunable resistive pulse sensing (TRPS)

The qNano Gold (Izon Sciences) was employed to quantify the size and concentration of EVPs via NP100 (50 – 330 nm) and NP600 (275 – 1570 nm) nanopore membranes. A pressure of 10 mbar and a voltage of 0.48 and 0.26 V was applied for the NP100 and the NP600, respectively. Polystyrene nanoparticles (CPC100 and CPC400) were used to calibrate the samples.

2.12 | Designing MBs

MBs (listed 5′−3′) targeting RNAs detected in this study are provided in Table S2. The designed MBs were custom synthesized and purified using high-performance liquid chromatography (HPLC; Integrated DNA Technologies, Coralville, IA). Locked nucleic acid nucleotides (depicted as +) were incorporated into the oligonucleotide strands to improve the thermal stability and nuclease resistance of the MBs for incubation at 37°C.

2.13 | siEVP capture using the ^{siEVP}PRA

0.1 mg/mL of NA was added to the chip and allowed to adsorb onto the photoetched micropatterns for 30 min. The chip was washed with PBS thoroughly to remove excess NA. A blocking solution of 3% BSA and 100 mg/mL of mPEG-SVA was added to avoid unwanted non-specific binding. Subsequently, a cocktail of biotinylated anti-CD63 and anti-CD9 were added at 10 μg/mL each and allowed to sit overnight at 4°C. For subpopulation-based sorting, anti-CD63, anti-CD9, anti-EGFR, anti-ARF6, anti-annexin A1, anti-ApoA1, anti-ApoB, and IgG were added separately at 20 μg/mL each or at 10 μg/mL each for cocktails, and allowed to sit overnight at 4°C. 3% BSA was added for 1 h to further block after washing away the capture antibodies. A

concentration of 10^9 particles/mL (apart from dilution experiments, which employed 0–10^{11} particles/mL) was then added and allowed to tether to the antibodies for 2 h at room temperature. Unbounded EVPs were washed away with PBS and further blocked with 3% BSA for 1 h.

2.14 | siEVP protein and RNA staining

About 10 μg/μL of MBs diluted in a 1× TE buffer were added to the immobilized siEVPs for 1 h at 37°C. As for protein detection, 0.4 μg/mL of the fluorescently labeled antibodies were diluted into a solution of 1% BSA was added to the EVP sample for 1 h at room temperature. Residual detection probes were washed away with PBS before imaging. For single biomarker analysis, sole detection probes were added. To analyze multiple proteins or RNAs, the probes were added sequentially, fluorescently labeled antibodies were added first, followed by MBs.

2.15 | Image analysis

Images of fluorescently labeled siEVPs were obtained by TIRFM (Nikon Eclipse Ti Inverted Microscope System) with a 100× oil immersion lens. An automatic algorithm was used to quantify the TIRFM images by detecting all bright signals determined via the defined outline of each bright signal by localizing the fluctuating fluorescence intensities throughout the image. The background noise was removed using a Wavelet de-noising method, and the net signal for all bright signals was obtained. The sum of all the bright signals within each micropattern was employed to calculate the total fluorescence intensity (TFI) of the sample alongside distributions of fluorescence intensity of the siEVPs. The TFI of samples was normalized to the average TFI of the negative controls as the RFI (Nguyen et al., 2022).

2.16 | ELISA

EGFR protein expression levels in Gli36-derived EVs were quantified using an EGFR Human ELISA kit (ThermoFisher Scientific). EVs were spiked in healthy donor serum at concentrations ranging from 0 to 10^{11} particles/mL while maintaining the serum-derived EVP concentration at 10^9 particles/mL. EGFR concentrations were quantified according to the manufacturer's instructions.

2.17 | qRT-PCR

cel-miR-39-3p levels within the engineered EVs were quantified using qRT-PCR. EVs were spiked in healthy donor serum at concentrations ranging from 0 to 10^{11} particles/mL while maintaining the serum-derived EVP concentration at 10^9 particles/mL. Total RNA from the EVPs was isolated and purified using an RNeasy Mini kit and a miRNeasy Serum/Plasma kit (Qiagen, Hilden, Germany), respectively, according to the manufacturer's instructions. cDNA was synthesized from the total RNA using a High-Capacity cDNA Reverse Transcription kit (Applied Biosystems, Foster City, CA) on a thermal cycler (Veriti 96-Well Thermal Cycler; Applied Biosystems). cel-miR-39-3p expression was quantified using a TaqMan Gene Expression assay (Assay Id: Hs01125301_m1; ThermoFisher Scientific) on a Real-Time PCR System (Applied Biosystems).

2.18 | Immunoblotting

Gli36 cells, Gli36-derived EV, serum-isolated VLDL/LDL, serum-isolated HDL, unprocessed serum, and TFF-purified serum samples were lysed in radioimmunoprecipitation assay (RIPA) buffer (ThermoFisher Scientific) with the addition of Pierce protease and phosphatase inhibitor (ThermoFisher Scientific) for 15 min on ice. Protein concentrations were quantified using a Micro BCA™ Protein Assay kit (ThermoFisher Scientific), according to the manufacturer's protocol. Equivalent amounts of sample proteins in a Laemmli buffer with 2-mercaptoethanol (MilliporeSigma) were electrophoresed on 4%–20% Mini-PROTEAN® TGX Stain-Free gels (Bio-Rad, Hercules, CA) and then transferred onto polyvinylidene fluoride (PVDF) membranes (Bio-Rad). The membranes were blocked and then probed with primary antibody diluted in tris-buffered saline with 0.1% Tween® 20 (TBS-T) overnight at 4°C and then with horseradish peroxidase (HRP)-conjugated secondary antibodies for 1 h at room temperature

(Table S1). Immunoreactivity was determined using enhanced chemiluminescence solutions (Bio-Rad) and visualized using a Bio-Rad ChemiDoc™ MP imaging system.

2.19 | Single-particle interferometric reflectance imaging sensing (SP-IRIS)

Silicon chips coated with tetraspanins (Unchained Labs, Boston, MA) were incubated for 1 h at room temperature with 5×10^8 Gli36-derived EVs diluted in a final volume of 60 μL of incubation buffer A. After the incubation, the silicon chips were washed 3 times for 3 min on an orbital plate shaker with wash solution B. The chips were scanned with the ExoView™ R200 reader (Unchained Labs) with the ExoScanner software (Unchained Labs). The particle size was allowed to scatter from 50 nm to 200 nm. The data was analyzed using ExoViewer software (Unchained Labs).

2.20 | Scanning electron microscopy (SEM)

Gli36-derived EVs were immobilized to the micropatterned coverslip overnight at 4°C. The immobilized siEVs were fixed in a 2% glutaraldehyde (MilliporeSigma) and 0.1 M sodium cacodylate solution (Electron Microscopy Sciences, Hatfield, PA) for 3 h. EVs were incubated in 1% osmium tetraoxide (Electron Microscopy Sciences) and 0.1 M sodium cacodylate for 2 h after washing with a 0.1 M sodium cacodylate solution. Subsequently, the sample was dehydrated with increasing ethanol concentrations (50, 70, 85, 95, and 100%) for 30 min each. Later, the CO_2 critical point dryer (Tousimis, Rockville, MD) was applied to dry the sample. Lastly, a ~2 nm layer of gold coating was deposited on the surface using a sputtering machine (Leica EM ACE 600, Buffalo Grove, IL) and was imaged using an SEM (Apreo 2, FEI Company, Hillsboro, OR).

2.21 | Transmission electron microscopy (TEM)

Two 20-μL DI water droplets and two 20-μL droplets of UranyLess EM contrast stain (Electron Microscopy Science) were placed on parafilm. TEM grids were plasma treated for 1 min before 10 μL of Gli36-derived EVs and serum-isolated LPs were drop cast onto the treated surface. The samples were incubated on the TEM surface for 1 min and then blotted away with filter paper. The TEM grids were washed immediately by dipping into the DI water droplet, blotting with filter paper, and repeating with the other droplet. The same technique was repeated for the contrast stain with 22 s incubations. The TEM grid was kept in the grid box overnight to completely dry before imaging. TEM imaging was carried out with a Tecnai TF-20 (FEI Company) operating at 200 kV.

2.22 | Cryogenic TEM (Cryo-TEM)

3-μL aliquots of EV samples with and without a 1× TE buffer incubated at 37°C for 2 h were added to lacey 300-mesh copper specimen grids (Product #01883; Ted Pella Inc., Redding, CA). Excess liquid was blotted away for 4 s with Whatman™ grade 1 filter papers (ThermoFisher Scientific), after which the grid was immediately plunged into liquid ethane with the Vitrobot Mark IV system (ThermoFisher Scientific) to rapidly form a thin layer of amorphous ice. The grid was then transferred under liquid nitrogen to a Glacios™ Cryo-TEM (ThermoFisher Scientific). Lastly, images were collected with a Felcon™ direct electron detector (ThermoFisher Scientific).

2.23 | RNA sequencing

RNA, including mRNA and miRNA, was isolated from cells and the cell-derived EVs using the miRNeasy kit (Qiagen). The RNA was eluted with 50 μL of nuclease-free water and the quality was assessed using an RNA (Pico) chip on an Agilent 2100 Bioanalyzer (Agilent Technologies, Santa Clara, CA). A sRNA-seq library construction method that utilizes adapters with four degenerated bases to reduce adapter-RNA ligation bias was used to characterize the miRNA (Etheridge et al., 2018). Size selection was performed using a Pippin HT automated size-selection instrument (Sage Science, Beverly, MA), and library concentrations were measured with the NEBNext Library Quant kit (New England Biolabs, Ipswich, MA). The libraries were pooled to a final concentration of 2 nM and run on a NextSeq sequencer (Illumina, San Diego, CA). The sRNA-seq data was analyzed with sRN-Analyzer (Wu et al., 2017). The quantity of miRNA was determined based on the number of mapped reads that were normalized with Count Per Mapped Million (CPM). RNA from cells and EVs were analyzed using Agilent Human Whole Genome 8×60 microarrays with fluorescent probes prepared from isolated RNA samples using Agilent QuickAmp Labeling kit according to the

manufacturer's instructions (Agilent). Gene expression information was obtained with Agilent's Feature Extractor and processed with the in-house SLIM pipeline (Marzolf & Troisch, 2006).

2.24 | Colocalization efficiency

An open-source plugin for ImageJ called EzColocalization was employed to visualize and measure the colocalization of EV biomarkers from acquired TIRFM images (Stauffer et al., 2018).

2.25 | Statistical analysis

Statistics were performed using the JMP Pro 14 software (JMP, Cary, NC), whereby statistical significances were inferred with the satisfaction of $p < 0.05$. Data are expressed as the mean ± SD.

3 | RESULTS

3.1 | siEVP analysis with the ^{siEVP}PRA

The ^{siEVP}PRA was fabricated with the PRIMO optical module (Figure 1a). Glass coverslips were coated with poly-L-lysine (PLL) through physisorption. Methoxy-poly(ethylene glycol)-succinimidyl valerate (mPEG-SVA) was covalently bound to the surface through N-hydroxysuccinimide (NHS) chemistry, creating a non-biofouling surface. A five-by-five array of 20-μm diameter circles was photoetched from the mPEG monolayer via UV projections translated by a digital-micromirror device (DMD) in the presence of 4-benzoylbenzyl-trimethylammonium chloride (PLPP) as a photoactivator (Figure 1a-i). The photoetching of the mPEG monolayer promotes the adsorption of proteins (Strale et al., 2016), such as NeutrAvidin (NA), that can further be functionalized via biotin motifs. Therefore, biotinylated antibodies against surface proteins expressed on EVPs were immobilized strictly within the micropatterns to selectively sort siEVPs (Figure 1a-ii). siEVP proteins were tagged with fluorescently labeled antibodies, while RNA species, including mRNAs and miRNAs, were tagged with MBs (Figure 1a-iii). Lastly, TIRFM was utilized to visualize the signals from immobilized siEVPs, as TIRFM produces an exponentially decaying electromagnetic wave that only excites fluorophores near the glass surface. The micropattern-based design thus allows for a facile multiplexed analysis of siEVPs by immediately identifying and colocalizing signals in different regions of the glass surface.

The photoetching level correlates to the grayscale value of a digital template and the UV dose (Strale et al., 2016). Therefore, various configurations of grayscale and dose were tested to generate micropatterns to maximize siEVP signals and minimize noise. EVs were harvested from Gli36 cells, a human glioma cell line, which were grown in serum-free media to minimize LP-EV interactions during EV collection (Busatto et al., 2022). The collected EVs, purified by tangential flow filtration (TFF) (Zhang et al., 2021), alongside a negative control, phosphate-buffered saline (PBS), were tested on the various micropattern configurations, which were functionalized with antibodies targeting CD63 and CD9, common membrane proteins constitutively expressed in various subpopulations of EVs (Kowal et al., 2016). The captured EVs were then detected with a fluorescently labeled antibody against CD63. A 50% grayscale value and a 20 mJ/mm^2 dose rendered the highest fluorescence intensity on siEVs relative to the control and minimized the non-specific binding of the fluorescently labeled antibody to the micropatterns (Table S3). Furthermore, the optimized grayscale value and dose demonstrated the homogenous adsorption of NA with specificity to the photoetched micropatterns (Figure S1).

To detect the presence of RNA within siEVs tethered to the micropatterns, a fluorescently labeled antibody against CD63 and a MB targeting hsa-miR-21-5p, an abundant vesicular miRNA in GBM (Abels et al., 2019; Akers et al., 2013), were used as detection probes simultaneously, and visualized via TIRFM. Each green signal represented a siEV expressing CD63, while each red signal represented a siEV carrying hsa-miR-21-5p in the acquired TIRFM images. Each yellow signal thus demonstrated the colocalization of both biomarkers. Conversely, fluorescence signals in the control were significantly lower, indicating the ability of ^{siEVP}PRA to selectively multiplex different biomolecular species in siEVs (Figure 1b). Furthermore, the TIRFM images could be quantified as distributions of fluorescence intensity of the siEVs to analyze the heterogenous expression of biomarkers on siEVs (Figure 1c) or to quantify and statistically compare various samples utilizing relative fluorescence intensities (RFI; the total fluorescence intensity of signals detected in the sample divided by the average total fluorescence intensity of signals detected in PBS within the five-by-five array):

$$TFI = \sum_{i=1}^{25}\left(\sum_{j=1}^{n} s_j\right)_i \qquad RFI = \frac{TFI_{EVP}}{\langle TFI_{PBS}\rangle} \tag{1}$$

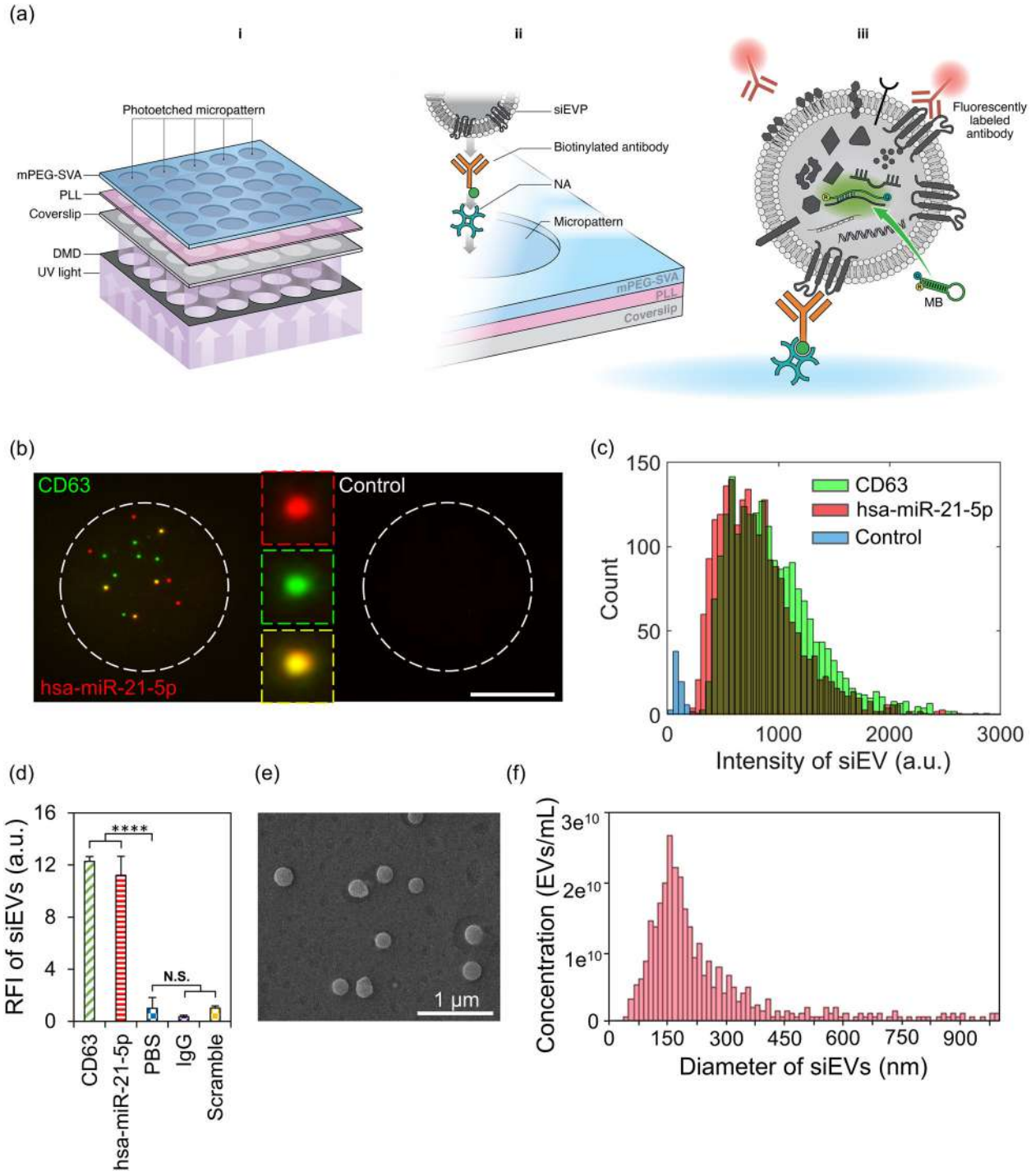

FIGURE 1 Detection of siEVPs with the ^{siEVP}PRA. (a) A schematic representation of the assay is condensed into three steps: (i) ^{siEVP}PRA fabrication in which coverslips functionalized with poly-L-lysine (PLL) and subsequently methoxy-poly(ethylene glycol)-succinimidyl valerate (mPEG-SVA) are photoetched into micropattern arrays using a digital-micromirror device (DMD) UV projection system, (ii) single extracellular vesicle and particle (siEVP) capture in which NeutraAvidin (NA) is physisorbed onto the micropattern arrays to immobilize biotinylated antibodies against epitopes on the surfaces of siEVP to sort and capture siEVPs, and (iii) detection of multiple biomolecular species on siEVPs in which fluorescently labeled antibodies and molecular beacons (MBs) are utilized to detect proteins and RNAs, respectively, via total internal reflection fluorescence microscopy (TIRFM). (b) CD63 (green dots) and hsa-miR-21-5p (red dots) on Gli36-derived single EVs (siEVs) are detected and colocalized (yellow dots) with the ^{siEVP}PRA. The control sample (phosphate-buffered saline; PBS) demonstrates a negligible fluorescence signal. (c) TIRFM images are quantified as distributions of fluorescence intensity to depict the expression of CD63 and hsa-miR-21-5p at a single-particle level for the different samples. (d) TIRFM images are quantified as bar graphs of relative fluorescence intensity (RFI) for CD63 and hsa-miR-21-5p in siEVs captured in the device and the negative controls, including PBS, IgG, and scramble ($N = 4$, error bars indicate the standard deviation, $^{****}p < 0.0001$). (e) Scanning electron microscopy (SEM) of Gli36-derived EVs added to the ^{siEVP}PRA confirms the presence of siEVs immobilized on the micropatterned surface. (f) The size distribution and concentration of Gli36-derived siEVs measured by tunable resistive sense pulsing (TRPS). All micropatterns were functionalized with an anti-CD63/CD9 antibody cocktail, and all scale bars are 10 μm unless stated otherwise.

where TFI is the total fluorescence intensity, s is the fluorescence intensity from the j^{th} signal, and n is the number of signals within the i^{th} micropattern. The RFIs of siEVs for CD63 and hsa-miR-21-5p were 12.28 ± 0.37 and 11.21 ± 1.45, respectively (Dunnett's test, $p < 0.0001$ for CD63 and hsa-miR-21-5p), whereas IgG capture and detection for scramble miRNA produced negligible signals (Figure 1d; Dunnett's test, $p = 1.00$ for IgG and $p = 0.60$ for scramble). Therefore, CD63/CD9-mediated capture was used hereafter to test the sensitivity, specificity, and colocalization of signals. After EV immobilization, scanning electron microscopy (SEM) was performed on the device to further validate the fluorescence signals observed on the micropatterns as originating from siEVs. The SEM images revealed single, round particles, confirming the presence of siEVs tethered on the micropatterns (Figure 1e). TRPS measurements on the Gli36-derived EV sample used for the ^{siEVP}PRA demonstrated a mean-siEV diameter of ~150 nm (Figure 1f), consistent with the size of the vesicles observed by SEM. Thus, the ^{siEVP}PRA selectively captures siEVs within the micropatterns and multiplexes protein and RNA signals via immunoaffinity and MB hybridization.

3.2 | Specificity and sensitivity of RNA detection in siEVs

Although various methods are available to detect proteins on siEVPs, detecting RNA at a single-particle resolution without altering or damaging the integrity of the vesicles remains challenging (Hilton & White, 2021; Mateescu et al., 2017). Therefore, we aimed to optimize the specificity and sensitivity of RNA detection in siEVs from Gli36 cells with the ^{siEVP}PRA. To detect vesicular RNA, MBs were diluted in a tris-ethylenediaminetetraacetic acid (TE) buffer that is frequently used to solubilize and protect nucleic acids against degradation. On the other hand, TE contains ethylenediaminetetraacetic acid (EDTA), which electrostatically intercalates into the lipid bilayer causing its fluidization (Prachayasittikul et al., 2007), and a tris buffer, which synergizes with EDTA (Vaara, 1992). Therefore, we hypothesized that TE buffer may be used to stabilize the MBs and partially permeabilize the lipid bilayer of siEVs, allowing the MBs to reach the lumen of intact siEVs and hybridize with the desired RNA sequences. To test this, both the integrity of siEVs and the specificity of probes to intraluminal targets post-treatment with the TE buffer were quantified. The changes in EV concentration when incubating in the TE buffer and PBS were negligible when incubated at 4°C (Student's two-tailed t-test, $p = 0.88$) and 37°C (Student's two-tailed t-test, $p = 0.65$), implying the extent of permeabilization by the TE buffer neither induced aggregation nor dissolved the vesicular structures (Figure S2A). Furthermore, cryogenic TEM (cryo-TEM) revealed that the TE buffer did not compromise the lipid bilayer present on large and small EVs (Figure S2B). To ensure the specificity of the MBs to the desired intraluminal RNA targets with the ^{siEVP}PRA, hsa-miR-21-5p, a miRNA abundant in *Homo sapiens*, and cel-miR-39-3p, a non-human miRNA abundant in *Caenorhabditis elegans* (Madadi & Soleimani, 2019), were tested in siEVs derived from Gli36 cells. Gli36-derived siEVs detected with MBs targeting hsa-miR-21-5p exhibited single fluorescent signals within the micropattern when diluted in the TE buffer (Figure S3A). The MB formulation diluted in the TE buffer produced a fluorescence signal that was 6.83 ± 0.57 times higher than the formulation without the TE buffer (Tukey's HSD, $p = 0.0002$), indicating the necessity for partial permeabilization. Furthermore, the siEV signals obtained from partial permeabilization with the TE buffer were 9.57 ± 0.95 times higher than the negative control (Tukey's HSD, $p = 0.0002$), ensuring the specificity of the MB to intraluminal hsa-miR-21-5p. In contrast, Gli36-derived siEVs detected with MBs targeting cel-miR-39-3p within the TE buffer and PBS demonstrated a negligible difference when compared to their respective controls (ANOVA, $p = 0.82$), thus demonstrating the ability of ^{siEVP}PRA to target specific RNA sequences within partially permeabilized siEVs (Figure S3B). Furthermore, internal protein epitopes were enhanced with partial permeabilization (Student's two-tailed t-test, $p < 0.0001$), while external membrane protein detection after partial permeabilization was significantly similar (Student's two-tailed t-test, $p = 0.12$), indicating that partial permeabilization preserved protein signals necessary for colocalization analyses (Figure S3C). Therefore, the TE buffer partially permeabilizes the lipid bilayer of siEVs via membrane fluidization ensuring the integrity of siEVs and the delivery of probes into the lumen of intact siEVs.

To evaluate the robustness of RNA specificity using ^{siEVP}PRA, Gli36 cells were transfected via electroporation to express the non-human miRNAs: cel-miR-39-3p, cel-miR-54-3p, and cel-miR-238-3p (Figure S4A) (Mitchell et al., 2008; Vigneron et al., 2016). siEVs harvested from the transfected cells were then detected with MBs targeting cel-miR-39-3p, cel-miR-54-3p, and cel-miR-238-3p. The engineered siEVs enriched with non-human miRNAs were successfully detected as single fluorescent signals within the micropatterns with MBs targeting the corresponding miRNA, while control samples showed a negligible number of signals (Figure 2a). To ascertain a lack of cross-reactivity between the MBs and the other non-human miRNA, the three different engineered siEVs were tested against all the MBs targeting the non-human miRNA. Only the MBs targeting the corresponding non-human miRNA enriched within the engineered siEVs could be detected, whereas all disparate MBs presented a background level of signals (Figure S4B). Similarly, siEVPs purified from healthy donor serum presented few signals utilizing the MBs targeting non-human miRNA (Figure S4B). Specifically, cel-miR-39-3p-enriched siEVs detected by MBs targeting cel-miR-39-3p exhibited a RFI of 9.10 ± 2.07, while serum-derived siEVPs and the disparate MBs produced an average RFI of 1.08 ± 0.11 (Figure 2b; Dunnett's test, $p < 0.0001$ for the corresponding MB, $p = 1.00$ for serum-derived siEVPs and all disparate MBs); cel-miR-54-3p-enriched siEVs detected by MBs targeting cel-miR-54-3p exhibited a RFI of 9.43 ± 1.68, while serum-derived siEVPs and the disparate MBs produced an average RFI of 1.14 ± 0.15 (Figure 2b; Dunnett's test, $p < 0.0001$ for the corresponding MB, $p > 0.96$ for serum-derived siEVPs and all disparate MBs); and cel-miR-238-3p-enriched siEVs detected by MBs targeting

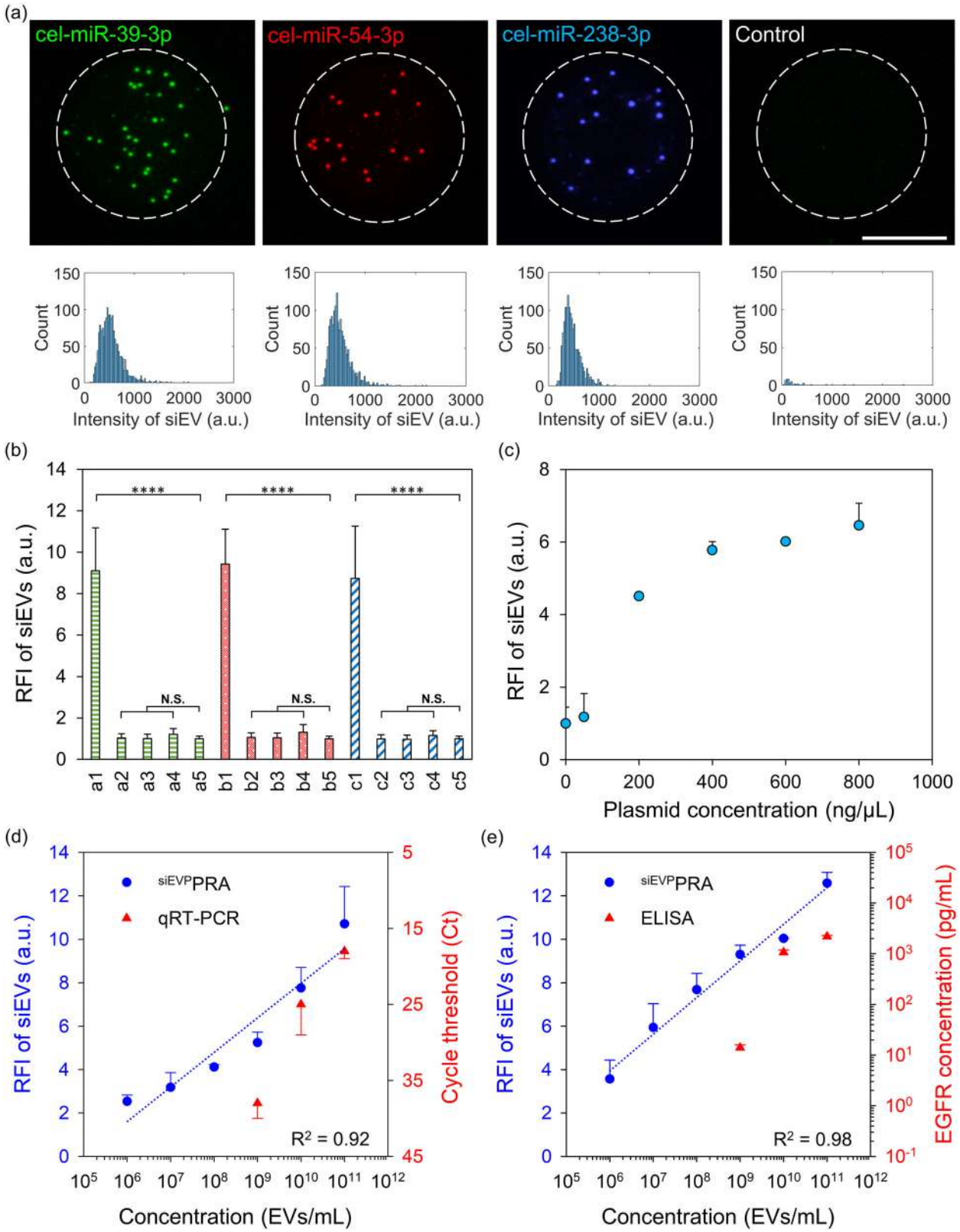

FIGURE 2 Specificity and sensitivity of RNA and protein detection in siEVs. (a) siEVs enriched with cel-miR-39-3p, cel-miR-54-3p, and cel-miR-238-3p are detected by the corresponding MBs targeting cel-miR-39-3p (green), cel-miR-54-3p (red), and cel-miR-238-3p (blue), whereas control samples demonstrate negligible fluorescence signal. (b) Bar graphs of the RFIs of siEVs with cel-miR-39-3p, cel-miR-54-3p, and cel-miR-238-3p with their corresponding MBs are higher than the different control conditions tested, including siEVs detected with unmatched MBs (a/b/c2, a/b/c3), siEVPs from human serum (a/b/c4), and PBS (a/b/c5). The denotations are provided in Figure S4 ($N = 3$, error bars indicate the standard deviation, ****$p < 0.0001$). (c) The RFI for the detection of cel-miR-39-3p in the engineered siEVs increases with increasing concentrations of the cel-miR-39-3p plasmid transfected into the cells ($N = 3$, error bars indicate the standard deviation). (d) The ^{siEVP}PRA is compared against standard qRT-PCR for cel-miR-39-3p from the engineered EVs secreted

(Continues)

FIGURE 2 (Continued)
from transfected Gli36 cells with a plasmid concentration of 400 ng/μL ($N = 3$, error bars indicate the standard deviation). The dotted line illustrates the linear fitting of the linear range ($R^2 = 0.92$; ANOVA, $p = 0.0026$). Representative images and distributions of fluorescence intensity are provided in Figure S5. (e) The ^{siEVP}PRA is compared against a standard ELISA for detecting EGFR from EVs isolated from Gli36 cells ($N = 3$, error bars indicate the standard deviation). The dotted line illustrates the linear fitting of the linear range ($R^2 = 0.98$; ANOVA, $p = 0.0001$). Representative images and distributions of fluorescence intensity are provided in Figure S6. All micropatterns were functionalized with an anti-CD63/CD9 antibody cocktail, and all scale bars are 10 μm unless stated otherwise.

cel-miR-238-3p exhibited a RFI of 8.73 ± 2.52, while serum-derived siEVPs and the disparate MBs produced an average RFI of 1.03 ± 0.10 (Figure 2b; Dunnett's test, $p < 0.0001$ for the corresponding MB, $p = 1.00$ for serum-derived siEVPs and all disparate MBs). Furthermore, the ^{siEVP}PRA could discriminate between the siEVs secreted from cells transfected with varying plasmid concentrations with the EV concentration held at a constant 10^9 particles/mL insofar as the RFI of the siEVs correlated positively with increasing plasmid concentrations (Pearson's correlation coefficient, $p < 0.0001$ for $r = 0.90$), demonstrating the sensitivity of the assay to quantify nucleic acid concentrations within siEVs (Figure 2c).

Provided the high sensitivity for detecting vesicular RNA, we compared the ^{siEVP}PRA against the benchmark method for bulk RNA detection, qRT-PCR. EVs harvested from Gli36 cells enriched with 400 ng/μL of the cel-miR-39-3p plasmid were diluted serially into EVPs isolated from healthy donor serum and were detected with the ^{siEVP}PRA and qRT-PCR for cel-miR-39-3p. The ^{siEVP}PRA exhibited a linear range at 10^6–10^{11} vesicles/mL ($R^2 = 0.92$; ANOVA, $p = 0.0026$), outperforming qRT-PCR, which became undetectable below a concentration of 10^9 vesicles/mL (Figure 2d). Events of non-specificity of the siEVs were observed outside the micropatterns only at the higher end of the dilutions, likely due to saturation of the micropattern (Figure S5A). Furthermore, the maxima in the fluorescence intensity distributions of the siEVs remained consistent across the dilution, indicating the decrease in RFI as a direct measurement of the dilution of siEVs (Figure S5B). Similarly, the sensitivity of the ^{siEVP}PRA for protein detection in siEVs was compared to ELISA, the benchmark bulk-analysis method. Gli36-derived EVs were diluted serially into EVPs isolated from healthy donor serum and were detected with both methods for a cytoplasmic epitope of EGFR, a transmembrane protein upregulated in GBM-associated EVs with external and intraluminal epitopes (Reátegui et al., 2018). Again, the ^{siEVP}PRA exhibited a linear range at 10^6–10^{11} vesicles/mL ($R^2 = 0.98$; ANOVA, $p = 0.0001$), whereas ELISA could not detect EGFR below a concentration of 10^9 vesicles/mL (Figure 2e) with similar observations to RNA detection (Figure S6A,B). Thus, the ability of the ^{siEVP}PRA to focus intact siEVs and highlight biomarkers of interest at minimal concentrations affords a unique ability to colocalize biomolecular species on siEVs and explore intravesicular heterogeneity, which cannot be realized by bulk-analysis methods.

3.3 | Simultaneous detection of various biomolecular species in siEVs

To first determine the ability of the ^{siEVP}PRA to multiplex various probes at a single-particle resolution, a tetraspanin analysis was performed on the siEVs, a commonplace procedure for in situ screening of siEVs (Han et al., 2021; Lee et al., 2018; Mizenko et al., 2021; Rima et al., 2022; Spitzberg et al., 2023). Therefore, Gli36-derived siEVs were screened for CD63, CD9, and CD81 with fluorescently labeled antibodies targeting the respective tetraspanins, whereby each antibody was chosen to excite at distinct wavelengths. The fluorescence signals were pseudo-colored as the primary colors of light such that the colocalization of two detection probes could be visualized as magenta, cyan, and yellow signals, while white signals illustrated the colocalization of all detection probes (Figure 3a). Furthermore, the fluorophores only emitted light when matched by their corresponding excitation wavelengths (Tukey's HSD, $p < 0.0001$ for the matched channels with siEVs only), ensuring the validity of the colocalization as originating from the co-expression of the tetraspanins (Figure S7). Figure 3b shows the colocalization efficiencies for CD63 and CD9 (20.08 ± 2.09%), CD81 and CD9 (19.31 ± 1.59%), CD63 and CD81 (20.84 ± 2.52%), and all three proteins (2.16 ± 0.58%). As mentioned earlier, various methods exist to simultaneously detect proteins on siEVs, such as single-particle interferometric reflectance imaging sensing (SP-IRIS) (Arab et al., 2021; Breitwieser et al., 2022; Deng et al., 2022). Therefore, we compared the ^{siEVP}PRA with a commercial SP-IRIS, the ExoView. Both the ^{siEVP}PRA and the ExoView produced similar signals whereby the colocalization of the tetraspanins was illustrated as yellow, magenta, cyan, and white (Figure S8A). Similar to the ^{siEVP}PRA, the ExoView differentiated positive signals from their isotype control at lower signal-to-noise ratios due to high levels of non-specificity (Figure S8B). Although the colocalization profiles are higher on the ExoView, interestingly, the highest frequency of colocalization tends to be the complementary color to the antibody used to capture the siEVs; specifically, $CD9^+/CD81^+$ siEVs for CD63-mediated capture, $CD63^+/CD81^+$ siEVs for CD9-mediated capture, and $CD9^+/CD63^+$ siEVs for CD81-mediated capture (Figure S8C). Using an antibody cocktail as performed with the ^{siEVP}PRA appears to normalize the bias to the capture antibody (Figure 3b; Levene's test, $p = 0.0049$). While the colocalization frequencies are higher on the ExoView, the ^{siEVP}PRA provides higher signal-to-noise ratios for protein detection (~12 for the ^{siEVP}PRA vs. ~3 for the ExoView), an ability to colocalize with nucleic acid cargo, working concentrations one order of magnitude lower, and multiple technical replicates for a reliable colocalization analysis.

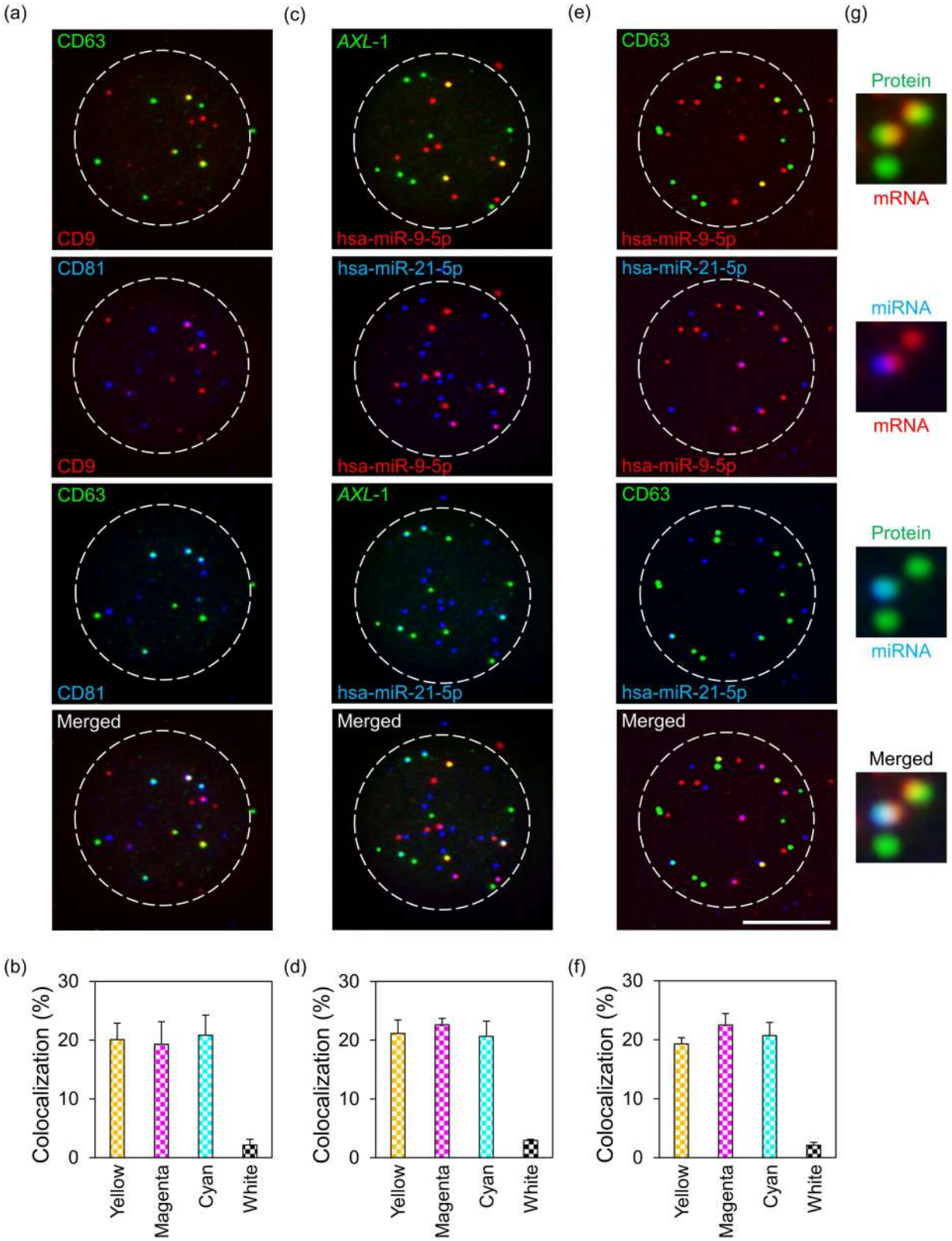

FIGURE 3 Multiplexed detection of siEVs across various biomolecules. (a) The colocalization of tetraspanins on Gli36-derived siEVs via multi-protein detection with the ^{siEVP}PRA show siEVs expressing CD63 (green), CD9 (red), CD81 (blue), CD63 and CD9 (yellow), CD9 and CD81 (magenta), CD81 and CD63 (cyan), and all three tetraspanins (white). (b) Bar graphs of the quantification of the colocalization rates of the tetraspanins are depicted with respect to their additive colors ($N = 3$, $n = 25$, error bars indicate the standard deviation). (c) The colocalization of multiple RNA species within Gli36-derived siEVs via multi-RNA detection with the ^{siEVP}PRA show siEVs expressing *AXL*-1 (green), hsa-miR-9-5p (red), hsa-miR-21-5p (blue), *AXL*-1 and hsa-miR-9-5p (yellow), hsa-miR-9-5p and hsa-miR-21-5p (magenta), hsa-miR-21-5p and *AXL*-1 (cyan), and all three RNA species (white). (d) Bar graphs of the quantification of the colocalization rates of the multiple RNA species are depicted with respect to their additive colors ($N = 3$, $n = 25$, error bars indicate the standard deviation). (e)

(Continues)

FIGURE 3 (Continued)

The colocalization of multiple biomolecular species within Gli36-derived siEVs via protein-RNA co-detection with the ^{siEVP}PRA show siEVs expressing CD63 (green), hsa-miR-9-5p (red), hsa-miR-21-5p (blue), CD63 and hsa-miR-9-5p (yellow), hsa-miR-9-5p and hsa-miR-21-5p (magenta), hsa-miR-21-5p and CD63 (cyan), and all three biomolecular species (white). (f) Bar plots of the quantification of the colocalization rates of the multiple biomolecular species are depicted with respect to their additive colors ($N = 3$, $n = 25$, error bars indicate the standard deviation). (g) Insets of the colocalization of protein, mRNA, and miRNA within Gli36-derived siEVs with the ^{siEVP}PRA show siEVs expressing CD63 (green), *AXL*-2 (red), hsa-miR-21-5p (blue), CD63 and *AXL*-2 (yellow), *AXL*-2 and hsa-miR-21-5p (magenta), hsa-miR-21-5p and CD63 (cyan), and all three biomarkers (white). The representative images from which the insets were derived and the quantifications thereof are presented in Figure S11. All micropatterns were functionalized with an anti-CD63/CD9 antibody cocktail, and all scale bars are 10 μm unless stated otherwise.

Although there are various methods to co-detect proteins on siEVs in situ, to our knowledge, the colocalization of RNAs in siEVs has not yet been achieved. Therefore, different regions of an mRNA strand were detected simultaneously within siEVs. Given the length of mRNA strands, three MBs were designed to emit distinct wavelengths when hybridized to different regions of the receptor tyrosine kinase *AXL* mRNA, which is abundant in GBM (Hutterer et al., 2008; Sadahiro et al., 2018). All three regions of the *AXL* mRNA were detected in siEVs as single fluorescent signals, which, similar to multi-protein detection, were pseudo-colored to reveal yellow, magenta, cyan, and white signals as colocalization events (Figure S9A). The distributions of fluorescence intensity for the single *AXL* regions detected by the MBs were similar (Figure S9B). Moreover, the RFIs of the three different regions on the *AXL* mRNA were negligibly different (ANOVA, $p = 0.51$), demonstrating a uniform and noncompetitive affinity of the MBs to the different regions of the mRNA strand (Figure S9C). Figure S9D shows the colocalization efficiencies for *AXL*-1 and *AXL*-2 (26.89 ± 2.61%), *AXL*-2 and *AXL*-3 (28.57 ± 3.24%), *AXL*-1 and *AXL*-3 (23.05 ± 6.21%), and all three regions (2.87 ± 1.03%). Having shown the ability to colocalize signals on the same RNA biomarker in siEVs with the ^{siEVP}PRA, we aimed to detect multiple distinct miRNAs and thus utilized the engineered EVs. Therefore, siEVs harvested from Gli36 cells transfected with cel-miR-39-3p, cel-miR-54-3p, and cel-miR-238-3p plasmids were detected by their respective MBs as was previously performed, but in conjunction, revealing the co-expression of multiple miRNAs within the same siEV (Figure S10A). Figure S10B shows the colocalization efficiencies for cel-miR-39-3p and cel-miR-54-3p (32.94 ± 1.47%), cel-miR-54-3p and cel-miR-238-3p (31.10 ± 1.03%), cel-miR-238-3p and cel-miR-39-3p (31.26 ± 2.90%), and all three miRNAs (5.51 ± 0.51%).

To add further complexity to the multiplexed RNA detection, multiple RNA species were screened in Gli36-derived siEVs. *AXL*-1, hsa-miR-9-5p, and hsa-miR-21-5p were colocalized in various siEVs revealing the co-expression of mRNA and miRNA (Figure 3c). Figure 3d shows the colocalization efficiencies for *AXL*-1 and hsa-miR-9-5p (21.15 ± 2.29%), hsa-miR-21-5p and hsa-miR-9-5p (22.62 ± 1.08%), *AXL*-1 and hsa-miR-21-5p (20.67 ± 2.58%), and all three RNA biomarkers (2.95 ± 0.18%). We then used the two methods of detection, immunoaffinity and MB hybridization, together to test the ability of the ^{siEVP}PRA to multiplex proteins and RNA simultaneously. Therefore, CD63, hsa-miR-9-5p, and hsa-miR-21-5p were screened in Gli36-derived siEVs, revealing colocalization (Figure 3e). Figure 3f shows the colocalization efficiencies for CD63 and hsa-miR-9-5p (19.30 ± 1.05%), hsa-miR-21-5p and hsa-miR-9-5p (22.52 ± 1.90%), hsa-miR-21-5p and CD63 (20.71 ± 2.23%), and all three biomarkers (2.12 ± 0.48%). Lastly, we aimed to detect protein, mRNA, and miRNA expression in Gli36-derived siEVs. The ^{siEVP}PRA successfully detected the co-expression of the three biomolecular species on siEVs (Figure 3g, Figure S11A). Figure S11B shows the colocalization efficiencies for CD63 and *AXL*-2 (21.49 ± 5.78%), hsa-miR-21-5p and *AXL*-2 (14.16 ± 2.84%), CD63 and hsa-miR-21-5p (13.68 ± 2.72%), and all three biomolecular species (0.43 ± 0.19%). Therefore, the marriage of the two detection methods on intact siEVs with the ^{siEVP}PRA broadens the horizon of current in situ methods, illustrating a rare display of siEV intravesicular heterogeneity with various biomolecular species.

3.4 | Sorting siEVPs into subpopulations

Tailoring the surface chemistry of the micropatterns enables the examination of intervesicular heterogeneity by first sorting siEVs into subpopulations based on membrane-protein composition. Although constitutively expressed, CD63 and CD9 are expressed in higher quantities in small EVs (Kowal et al., 2016) and are considered "classical" exosomal biomarkers due to their enrichment and involvement in cargo loading (Buschow et al., 2009; Chairoungdua et al., 2010; Escola et al., 1998; Théry et al., 1999; van Niel et al., 2011) despite being present in some ectosome subpopulations (Mathieu et al., 2021). On the other hand, ARF6 and annexin A1 are considered ectosomal biomarkers due to their enrichment and contribution towards the budding of vesicles from the plasma membrane (Clancy et al., 2019; Jeppesen et al., 2019; Muralidharan-Chari et al., 2009; Rogers et al., 2020). Moreover, Cetuximab, a chimeric monoclonal antibody, was utilized to capture tumor-specific siEVs, which targets the extracellular domain of EGFR and efficiently immobilizes tumor-derived EVs from GBM patients (Reátegui et al., 2018). WB analyses confirmed that tetraspanins CD63, CD9 and CD81 were enriched in the TFF-purified EVs from Gli36 cells when compared to their cellular concentrations. Conversely, EGFR, annexin A1, and ARF6 were upregulated in Gli36 cells, but were still present in the TFF-purified EVs (Figure 4a). Therefore, separate micropatterns were decorated with antibodies targeting CD63, CD9, annexin A1, ARF6, and EGFR with IgG as a negative isotype control for siEV capture. Two miRNAs (hsa-miR-21-5p and hsa-miR-9-5p), two mRNAs

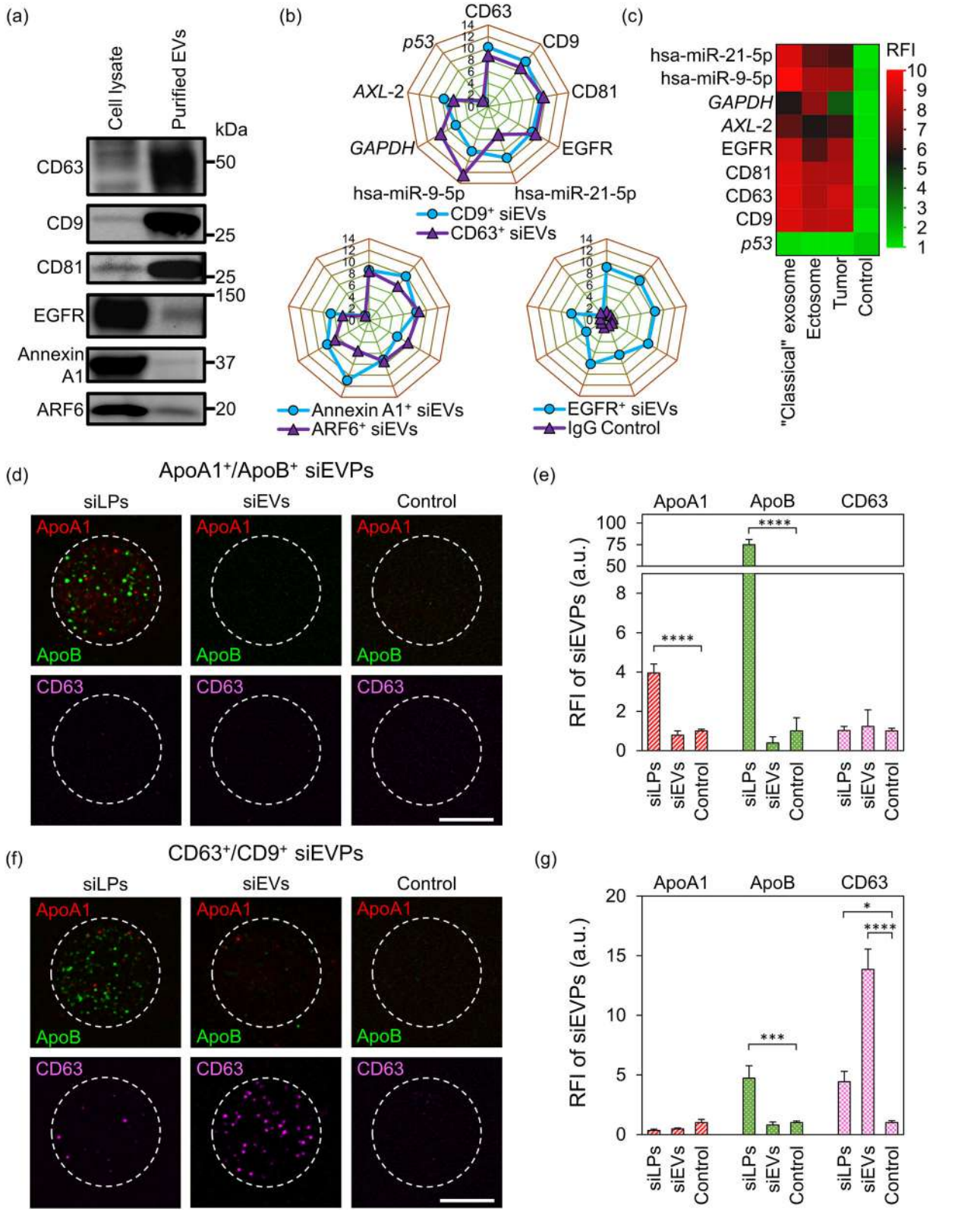

FIGURE 4 Single intervesicular and interparticle heterogeneity analysis. (a) Western blot (WB) analyses on CD63, CD9, CD81, EGFR, annexin A1, and ARF6 on cell and EV lysates. (b) Radar plots of the multidimensional data analysis of RFIs across multiple micropatterns functionalized solely with antibodies targeting CD9, CD63, annexin A1, ARF6, and EGFR with IgG as an isotype control, demonstrate variable detection levels for CD63, CD9, CD81, EGFR, hsa-miR-9-5p, hsa-miR-21-5p, *GAPDH*, *AXL*-2, *p53*. (c) A heatmap of the multidimensional data analysis after linear discriminant (Figure S11) and biogenesis pathways is condensed to demonstrate expression across clustered subpopulations, including "classical" exosomes, ectosomes, tumor-derived EVs, and an isotype control. (d) Single lipoproteins (siLPs) and siEVs are sorted on micropatterns functionalized with an anti-ApoB/ApoA1 antibody cocktail and detected for ApoA1 (red), ApoB (green), and CD63 (pink). (e) TIRFM images are quantified as bar graphs of the RFIs of the siEVPs for the $ApoB^+/ApoA1^+$

(Continues)

FIGURE 4 (Continued)
subpopulation ($N = 3$, error bars indicate the standard deviation, ****$p < 0.0001$). (f) siLPs and siEVs are sorted on micropatterns functionalized with an anti-CD63/CD9 antibody cocktail and detected for ApoA1 (red), ApoB (green), and CD63 (pink). (g) TIRFM images are quantified as bar graphs of the RFIs of the siEVPs for the $CD63^+/CD9^+$ subpopulation ($N = 3$, error bars indicate the standard deviation, ****$p < 0.0001$, ***$p < 0.001$, *$p < 0.05$). All scale bars are 10 μm unless stated otherwise.

(*GAPDH* and *AXL*-2), four proteins (CD63, CD9, CD81, and EGFR), and a control for RNA detection (*p53*), a gene downregulated in GBM (McGillicuddy et al., 2009; Zhang et al., 2018), were screened individually across the several subpopulations. The expression profiles indicated variable levels across the subpopulations (Figure 4b), with IgG unable to immobilize siEVs independent of the detection probe utilized (ANOVA, $p = 0.14$ for RFI, $p = 0.97$ for the probe) and *p53* detection demonstrating negligible signals independent of the subpopulation analyzed (ANOVA, $p = 0.34$ for RFI, $p = 0.92$ for the subpopulation). Furthermore, linear discriminant analysis on the expression of the nine biomarkers demonstrated vast heterogeneity across the subpopulations with similarities amongst $ARF6^+$ and $CD9^+$ siEVs (Figure S12A). However, by combining the biomarkers into their respective biomolecular species, the linear discriminant analysis revealed similarities between $CD63^+$, $CD9^+$, and $EGFR^+$ siEV profiles, while $ARF6^+$ and annexin $A1^+$ siEVs demonstrated similarities (Figure S12B). Therefore, the average RFI of the nine biomarkers was analyzed with respect to biogenesis pathways and the clustering from the linear discriminant analysis as "classical" exosomes ($CD63^+/CD9^+$ siEVs), ectosomes ($ARF6^+$/annexin $A1^+$ siEVs), tumor-derived siEVs ($EGFR^+$ siEVs), and an isotype control (IgG), exhibiting an enrichment of most biomarkers in $CD63^+/CD9^+$ siEVs (Figure 4c). Therefore, an anti-CD63/CD9 antibody cocktail was utilized for the remainder of the investigation to immobilize siEVPs.

Given that particles present in the blood are abundantly LPs (Simonsen, 2017), cholesterol-transporting particles that are often co-isolated with EVs due to their similar sizes and densities (Simonsen, 2017; Sódar et al., 2016; Yuana et al., 2014), we next examined the interaction of the ^{siEVP}PRA with LPs. First, we tested whether TFF, a size-exclusion purification process that was utilized on the Gli36-derived EVs, could remove LPs from healthy donor serum. While efficient at removing soluble proteins and retaining particles (Figure S13A,B), the composition of the particles was uncertain. Accordingly, high-density LPs (HDL) and a mixture of very-low-density LPs (VLDL) and low-density LPs (LDL) were separated from the same healthy donor serum via dextran-based precipitation (Burstein et al., 1970). The isolated LPs demonstrated an absence of annexin A1, ARF6, CD63, and CD9, and an abundance of ApoA1 in the HDL fraction and ApoB in the VLDL/LDL fraction (Figure S13C), which are absent in Gli36 cells and their EVs (Figure S13D). Furthermore, the isolated LPs demonstrated dense morphologies as opposed to the classical "cup shapes" of EVs observed in TEM (Figure S13E). TFF on the healthy donor serum demonstrated enrichment of CD63, annexin A1, and ApoB and retention with a slight loss of ARF6, CD9, and ApoA1 (Figure S13C) indicating the co-isolation of LPs and EVs after TFF purification. Therefore, Gli36-derived EVs and a mixture of the two LP isolates were deposited on the ^{siEVP}PRA functionalized with an anti-ApoB/ApoA1 antibody cocktail and screened for ApoA1, ApoB, and CD63. Positive single fluorescent signals for the $ApoA1^+/ApoB^+$ siEVP subpopulation were obtained solely in the siLP mixture for ApoA1 (Dunnett's test, $p < 0.0001$ for siLPs, $p = 0.61$ for siEVs) and ApoB (Dunnett's test, $p < 0.0001$ for siLPs, $p = 0.97$ for siEVs), while CD63 was absent in all siEVP formulations (ANOVA, $p = 0.83$), indicating the specificity of ApoB and ApoA1 to siLPs (Figure 4d,e). Interestingly, the micropatterns functionalized with an anti-CD63/CD9 antibody cocktail yielded positive signals for ApoB in siLPs (Dunnett's test, $p = 0.0006$ for siLPs, $p = 0.89$ for siEVs) and CD63 in siLPs and siEVs (Dunnett's test, $p = 0.016$ for siLPs, $p < 0.0001$ for siEVs), indicating the complete specificity of Gli36-derived siEVs to the micropatterns functionalized with an anti-CD63/CD9 antibody cocktail and the rare presence of CD63-expressing siLPs with an affinity for CD63/CD9-mediated capture, which are obscured by the majority of LPs (Figure 4f,g). The presence of a rare subpopulation of siLPs is confirmed by the absence of CD63 in the ^{siEVP}PRA analysis of the $ApoA1^+/ApoB^+$ siLP subpopulation, representing the majority of siLPs, and the absence of CD63 and CD9 in the WB analysis of HDL and VLDL/LDL samples. However, the ability to enrich these complex subpopulations of siLPs via immunopositive selection, which are possibly EV-LP hybrids (Busatto et al., 2022; Busatto et al., 2020; Sódar et al., 2016) or co-isolated serum-derived EVs with apolipoprotein corona (Tóth et al., 2021; Wolf et al., 2022), highlights the benefit of the ^{siEVP}PRA for probing interparticle heterogeneity at minuscule quantities that are lost with bulk-analysis methods.

Due to the extensive characterization of apolipoprotein corona on EVs (Tóth et al., 2021), we investigated their presence with the ^{siEVP}PRA as a possibility for the observed siLP-EV co-isolates. Therefore, TFF-purified EVs harvested from Gli36 cells cultured in serum-free media were incubated in EV-depleted plasma (EVDP) and subsequently purified to remove soluble proteins and enrich the EVs with apolipoprotein corona (Figure S14A). The EVs incubated in EVDP were then introduced to the ^{siEVP}PRA with CD63/CD9-mediated capture and detected for ApoA1 and ApoB. While siEVs that were not incubated in EVDP produced negligible fluorescence signal utilizing the same conditions (Figure 4f,g) with RFIs of 0.78 ± 0.22 for ApoA1 (Student's two-tailed *t*-test, $p = 0.19$) and 0.80 ± 0.26 for ApoB (Student's two-tailed *t*-test, $p = 0.29$), siEVs incubated in EVDP produced positive fluorescence signals for ApoA1 and ApoB reminiscent of siEVP signals (Figure S14B). Furthermore, siEVs incubated in EVDP produced RFIs of 8.95 ± 2.33 for ApoA1 (Welch's two-tailed *t*-test, $p = 0.0274$) and 41.19 ± 11.63 for ApoB (Welch's two-tailed *t*-test, $p = 0.0265$), confirming the ability for apolipoproteins to adhere onto the EV surface (Figure S14C). Given the complete specificity of siEVs to anti-CD63/CD9 functionalized micropatterns and the rarity of the siLP-EV co-isolates that may simply be

siEVs disguised with apolipoprotein corona, we advanced the investigation to test the ability of the ^{siEVP}PRA to detect vesicular RNA in a complex biofluid notwithstanding the observed complexity of biological samples.

3.5 | Profiling siEVP RNA in glioma cell lines and GBM patient serum

To demonstrate the translational potential of ^{siEVP}PRA and incorporation of vesicular RNA biomarkers, we performed transcriptomic analyses on six different glioma cell lines (SF268, SF295, SF539, SNB19, SNB75 and U251) and their corresponding EVs collected from serum-free media and purified by TFF, via sRNA-seq and microarrays (Crouser et al., 2021; Etheridge et al., 2018; Fallen et al., 2018; Ghai et al., 2017; Giraldez et al., 2018; Wu et al., 2017). To represent the pathological heterogeneity of gliomas, we included astrocytoma, gliosarcoma, and glioblastoma cell lines. Several RNAs exhibited high concentrations in both cells and EVs with miRNA showing more differential expression (Figure 5a). Among the high-expressing RNAs analyzed, four transcripts, two mRNAs (*NSF* and *NCAN*) and two miRNAs (hsa-miR-9-5p and hsa-miR-1246-5p) were selected for further analysis, due to their previous association with GBM (Lou et al., 2019; Qiu et al., 2021; Su et al., 2017; Zottel et al., 2020). In general, the concentrations measured via microarrays of the four selected transcripts across the different glioma cell lines showed less variability than their corresponding EVs (Levene's test, $p = 0.0002$ for *NSF*, $p = 0.33$ for hsa-miR-9-5p, $p = 0.0008$ for *NCAN*, $p = 0.013$ for hsa-miR-1246-5p), indicating the differential packing of the RNA species across the cell lines (Figure 5b). The heterogeneity of these transcripts in EVs was further explored with the ^{siEVP}PRA at a single-particle resolution (Figure 5c). The RFI determined by the ^{siEVP}PRA correlated positively with the concentration of the transcripts in the EVs derived from the different glioma cell lines (Pearson's correlation coefficient, $p = 0.0001$ for $r = 0.70$); however, failed to correlate with the cellular concentrations (Pearson's correlation coefficient, $r = 0.16$). The discrepancy was also observed between cellular and vesicular concentrations with bulk RNA measurements (Pearson's correlation coefficient, $r = 0.01$), indicating the ability of ^{siEVP}PRA to coincide with bulk RNA detection. However, an advantage the ^{siEVP}PRA exhibits, which bulk RNA measurements cannot achieve, is quantifying the variability of biomolecular expression in siEVPs via fluorescence profiles. The distributions of siEV fluorescence intensity demonstrated a more homogeneous expression for the mRNAs than the miRNAs across the six cell lines (Figures S15–S18). Specifically, hsa-miR-9-5p cargo from SF268-, SF295-, SF539- and SNB75-derived siEVs indicated more heterogeneous profiles with distribution maxima shifted to the right (Figure S17). Similarly, hsa-miR-1246-5p cargo from SF268-, SNB75-, and SNB19-derived siEVs also demonstrated a heterogeneous expression with distribution maxima shifted to the right (Figure S18).

Having validated the GBM-associated vesicular RNA biomarkers across various cell lines, the ^{siEVP}PRA was used to characterize siEVPs from TFF-purified serum from GBM patients. For each individual, 20 μL of the purified serum was processed with the ^{siEVP}PRA. A cohort of 10 GBM patients and 10 age-matched healthy individuals were chosen for the investigation (Table S4). Although we demonstrated the presence of siLP-EV co-isolates in serum, higher frequencies of positive signals for *NSF*, hsa-miR-9-5p, *NCAN*, and hsa-miR-1246-5p were obtained from purified GBM patient serum in comparison to healthy donor serum (Figure 6a). Furthermore, RFIs of siEVPs from GBM patients were significantly higher for *NSF*, *NCAN*, hsa-miR-9-5p, and hsa-miR-1246-5p RNAs when compared to the siEVPs from purified healthy donor serum (Figure 6b; Mann-Whitney *U* test, $p = 0.0002$ for *NSF, NCAN* and hsa-miR-9-5p, $p = 0.0022$ for hsa-miR-1246-5p). Comparing the distributions of fluorescence intensity for the different RNA species revealed that siEVPs expressing *NSF* and *NCAN* presented more homogeneous fluorescence signals. In contrast, the distributions of fluorescence intensity for siEVPs expressing hsa-miR-9-5p and hsa-miR-1246-5p yielded broad distributions of fluorescence intensity with distribution maxima shifted to the right (Figure 6c), which agreed with our previous observation on the siEVs across the glioma cell lines. These findings confirm the ability of ^{siEVP}PRA to measure the intravesicular heterogeneity of RNA in siEVPs from complex biofluids, specifically serum, and its ability to discriminate GBM patients from healthy donors while conserving vesicular profiles. The success of this work and the tunability of the ^{siEVP}PRA opens the possibility for its potential application in liquid biopsy for cancer diagnoses in GBM and other diseases.

4 | DISCUSSION

The enhanced sensitivity of siEVP methods, the tunability of surface chemistry within the micropatterns, and the ability to multiplex across various biomolecular species realized by the ^{siEVP}PRA lends unique opportunities to investigate intravesicular, intervesicular, and interparticle heterogeneity at a single-particle resolution. Due to the inherent heterogeneity of EVPs and the abundance of LPs in circulation, it is necessary to decode the molecular profile of EVPs and advance technologies to distinguish EVs from LPs. Highly tunable multiplexed approaches, such as the ^{siEVP}PRA, can aid in the precise deconvolution of siEVPs. Various novel siEV technologies have adopted an in situ approach to characterize siEVs to visualize intravesicular heterogeneity via colocalization analyses (Arab et al., 2021; Breitwieser et al., 2022; Deng et al., 2022; Han et al., 2021; Lee et al., 2018; Mizenko et al., 2021; Rima et al., 2022; Spitzberg et al., 2023). The ^{siEVP}PRA is the first assay to demonstrate intravesicular heterogeneity across multiple biomolecular species with colocalization analyses, including protein and RNA, which was realized with a facile incubation with a TE buffer that stabilizes MBs, ensures the integrity of intact siEVs, preserves external epitopes, and

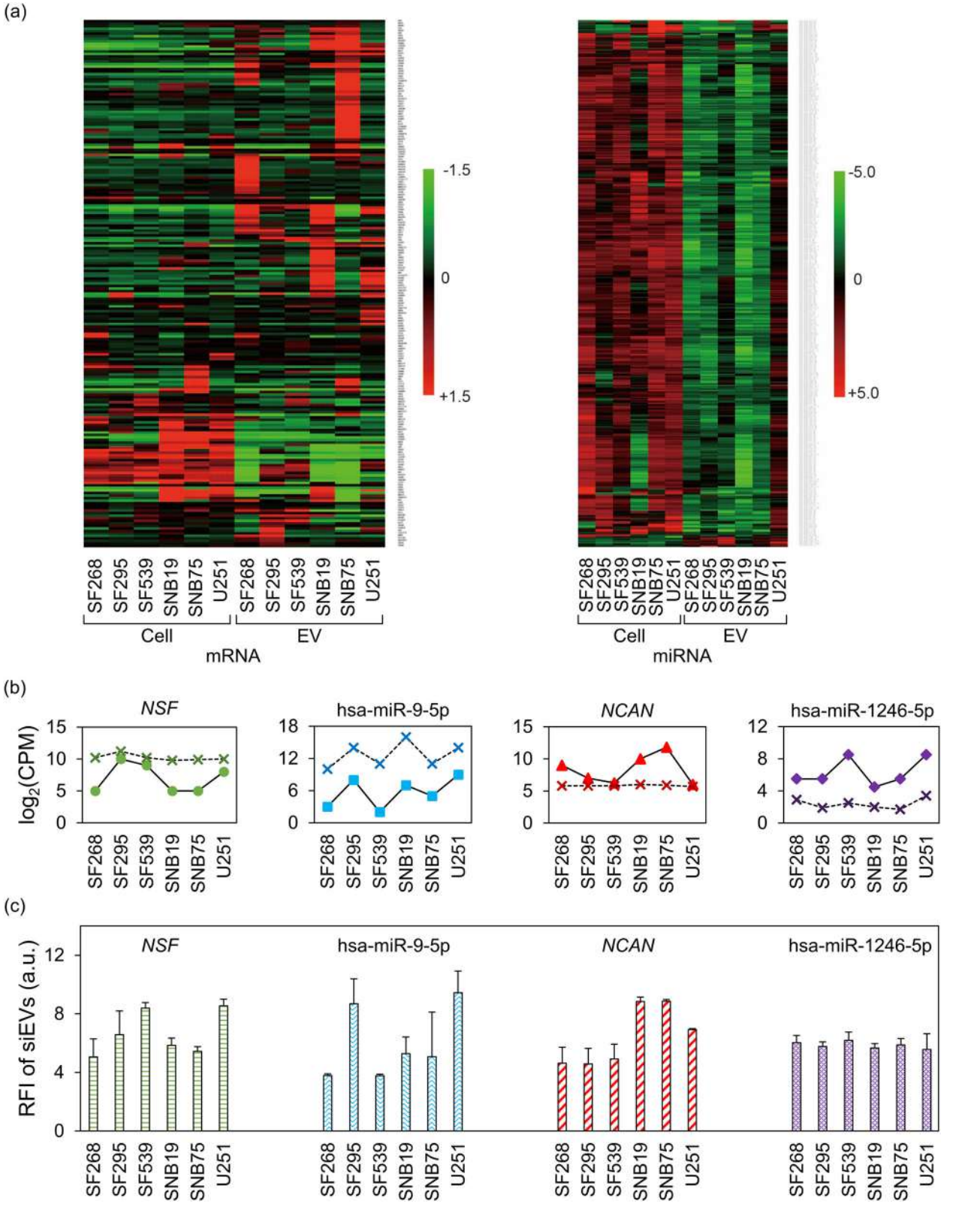

FIGURE 5 Sequencing of cellular and vesicular RNA in glioma cell lines and validation with the ^{siEVP}PRA. (a) Cellular and vesicular mRNA (left) and miRNA (right) are sequenced across six glioma cell lines, including SF268, SF295, SF539, SNB19, SNB75, and U251, revealing the upregulation of *NSF*, hsa-miR-9-5p, *NCAN*, hsa-miR-1246-5p in cells and EVs. (b) *NSF*, hsa-miR-9-5p, *NCAN*, and hsa-miR-1246-5p are profiled in EVs (solid line) and cells (dash line) from the six different glioma cell lines by bulk RNA characterization. (c) Bar graphs of the RFIs of *NSF*, hsa-miR-9-5p, *NCAN*, and hsa-miR-1246-5p in siEVs from the six different glioma cell lines with the ^{siEVP}PRA, showing comparable RNA expression trends ($N = 3$, error bars indicate the standard deviation). Representative images and distributions of fluorescence intensity are provided in Figure S15–S18. All micropatterns were functionalized with an anti-CD63/CD9 antibody cocktail.

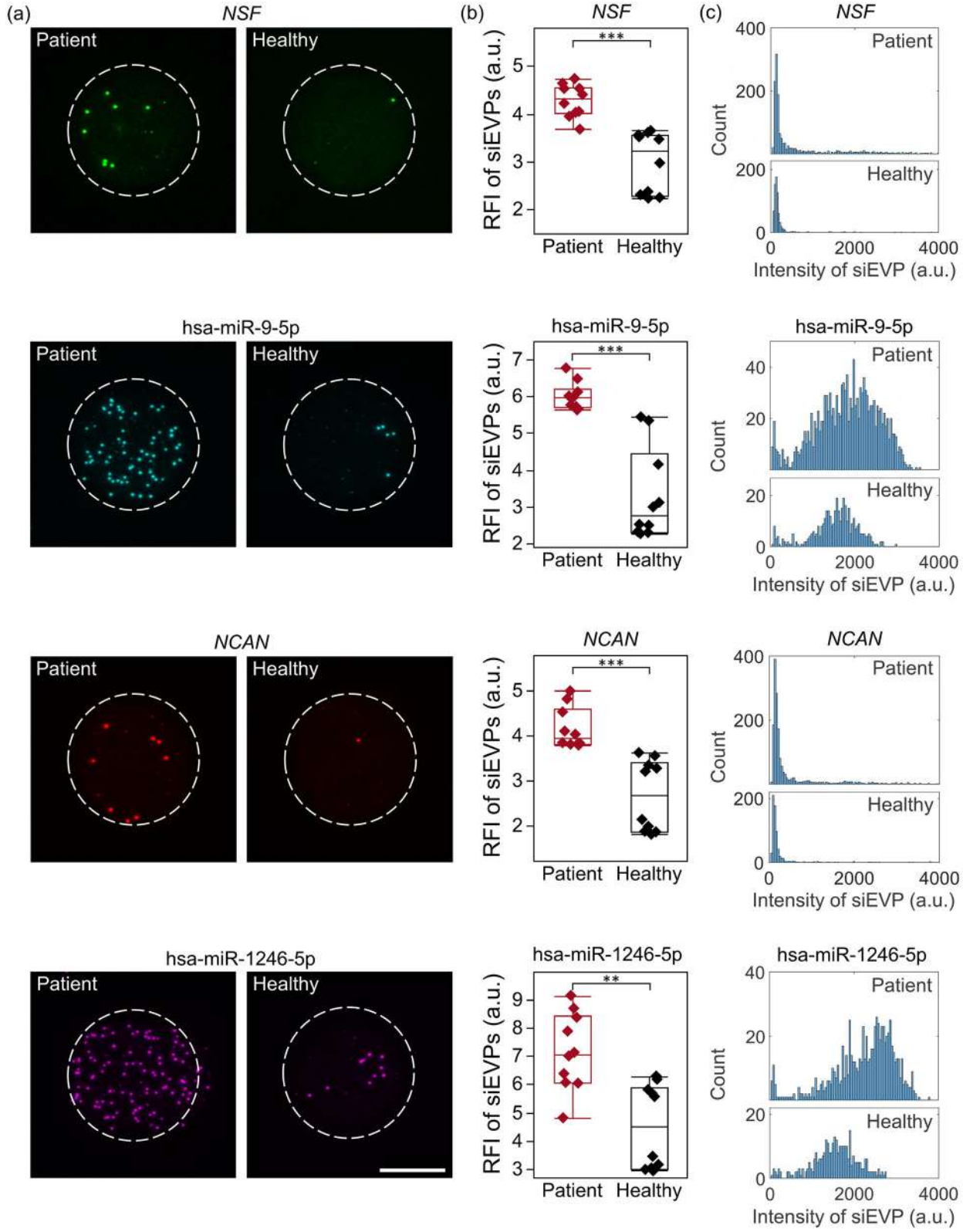

FIGURE 6 Differential expression of GBM-associated vesicular RNA species in siEVPs from GBM patient serum. (a) Representative TIRFM images of siEVPs expressing *NSF*, hsa-miR-9-5p, *NCAN*, and hsa-miR-1246-5p in TFF-purified serum from GBM patients and healthy donors characterized with the ^{siEVP}PRA. (b) Box plots of the RFIs for *NSF*, hsa-miR-9-5p, *NCAN*, and hsa-miR-1246-5p in GBM patients and healthy donors ($N = 10$, $^{***}p < 0.001$, $^{**}p < 0.01$). (c) Representative distributions of fluorescence intensity for the siEVP detection of *NSF*, hsa-miR-9-5p, *NCAN*, and hsa-miR-1246-5p in TFF-purified serum from patient and healthy donors, indicate variable expression and homogenous profiles amongst mRNAs and heterogeneous profiles amongst miRNAs. All micropatterns were functionalized with an anti-CD63/CD9 antibody cocktail, and all scale bars are 10 μm unless stated otherwise.

delivers detection probes into the lumen of siEVs via partial permeabilization. While the highest colocalization rates were observed for the engineered siEVs, which is non-trivial due to the induced enrichment of synthetic miRNA species, the second-highest (highest non-synthetic) colocalization rate was observed for the co-detection of multiple regions of the *AXL* mRNA strand. Interestingly, only a small population of siEVs demonstrated the colocalization of all targets, further demonstrating the observed fragmentation of mRNA strands during packaging (Batagov & Kurochkin, 2013; de Voogt et al., 2021; Dellar et al., 2022; Hinger et al., 2018; Wei et al., 2017; Zand Karimi et al., 2022), which can compromise highly sensitive assays that require high-quality RNA, such as qRT-PCR (Antonov et al., 2005). Lastly, interspecies colocalization yielded similar colocalization rates, indicating consistency across methods, except for the co-detection of protein, mRNA, and miRNA, which demonstrated slightly lower frequencies of mutual expression. While often utilized for colocalization analyses, we found that colocalization was relatively low for the tetraspanins, which agrees with other reported siEV tetraspanin analyses (Han et al., 2021; Lee et al., 2018; Rima et al., 2022; Spitzberg et al., 2023). With the ^{siEVP}PRA, we could further observe intravesicular heterogeneity for single biomolecular expression as fluorescence intensity distributions. As such, we observed higher miRNA variability than mRNA in the siEVs secreted from the glioma cell lines and siEVPs in GBM patient serum. Due to the small size of intact miRNA (~22 nucleotides) (Dellar et al., 2022) and the fragmentation of mRNA in EVs (Batagov & Kurochkin, 2013; de Voogt et al., 2021; Dellar et al., 2022; Hinger et al., 2018; Wei et al., 2017; Zand Karimi et al., 2022), the observed variability in miRNA may be a more accurate illustration of non-genetic single-cellular heterogeneity (Wang et al., 2019). Both methods to profile intravesicular heterogeneity were lost with bulk-analysis methods, such as WB, ELISA, qRT-PCR, sRNA-seq, and microarrays, indicating the utility of the ^{siEVP}PRA in uncovering intravesicular heterogeneity.

Intervesicular and interparticle heterogeneity were recognized by tuning the surface chemistry on the micropattern within the ^{siEVP}PRA to capture siEVP subpopulations. Testing various capture antibodies and detection probes on Gli36-derived siEVs further elucidated intervesicular heterogeneity between subpopulations as a function of biomarker expression. Multivariate analyses on the grouped biomolecular species revealed similar profilometric trends for $CD63^+$, $CD9^+$, and $EGFR^+$ siEV subpopulations, which corresponds with the upregulation of EGFR in Gli36-derived "classical" exosomes (Jeppesen et al., 2019). Furthermore, capturing siEVs by CD63 and CD9 yielded the most holistic signature across all biomolecules tested, which coincides with immunoselective immobilization strategies for siEVPs from non-small cell lung cancer patient serum (Nguyen et al., 2022). A possibility for the enhanced capture and detection utilizing an anti-CD63/CD9 antibody cocktail to immobilize siEVs may be that the cocktail does not discriminate cellular origin and rather captures siEVs from all cells. While originally considered a "classical" exosomal biomarker, CD9 is present in larger EVs albeit enriched in small EVs (Kowal et al., 2016), and is found on small ectosomes (Mathieu et al., 2021). Interestingly, our linear discriminant analysis on the single biomarker expression demonstrated similarities between $CD9^+$ and $ARF6^+$ siEV subpopulations. Therefore, the anti-CD63/CD9 antibody cocktail may capture exosomes and ectosomes, thus widening the breadth of capture. However, the antibody cocktail was insufficient in sorting out LPs as we uncovered $CD63^+/CD9^+$ siLP-EV co-isolates, concurring with newer evidence on the complexity of LPs and EVs (Busatto et al., 2022; Busatto et al., 2020; Sódar et al., 2016; Tóth et al., 2021; Wolf et al., 2022). Specifically, we were able to confirm the co-expression of ApoA1 and ApoB on the surface of EVs as protein corona with the ^{siEVP}PRA (Tóth et al., 2021), which may maintain bioactivity and have implications in disease progression (Wolf et al., 2022). Various studies utilize tetraspanins to immobilize siEVs and assume negligible interactions with LPs. This erroneous assumption may result from the dilution of the subpopulation in bulk-analysis methods, further motivating the necessity for siEVP methods in uncovering interparticle heterogeneity.

Although the ^{siEVP}PRA is highly sensitive and capable of discerning heterogeneous subpopulations amongst siEVPs, colocalization is limited to the number of compatible fluorophores, indicating the possibility for siEVP subpopulations immobilized on the micropattern that downregulate all targets. With the inherent heterogeneity of blood-derived EVPs, capturing all signals could lead to a more comprehensive compositional analysis. Advances in spectral microscopy (Valm et al., 2016), sequential labeling (Chen et al., 2015), and quantum-dot synthesis (Chattopadhyay et al., 2006), to name a few, are strategic methods for overcoming spectral overlapping in bandpass filters, the applications of which could further increase the scope of targeted siEVPs. Furthermore, SP-IRIS demonstrated higher colocalization rates for the tetraspanin analyses, albeit with high levels of non-specificity. The use of enhancing methods, such as the incorporation of an interferometric substrate (Daaboul et al., 2010) or surface plasmon resonating surfaces (Im et al., 2014; Nguyen et al., 2022), can further increase signals but would require complex micropattern synthesis techniques that may limit their facile distribution and low cost. Lastly, we found a complex subpopulation of siLP-EV co-isolates, which may competitively interact with the micropatterned surface. While their presence indicated minimal interference with the capability of the ^{siEVP}PRA to measure GBM-associated vesicular RNA profiles in GBM patient serum, we cannot dismiss the possible contributions of siLPs as RNA carriers (Vickers et al., 2011). Future investigations aim at a detailed profiling of the complex subpopulation of siLPs.

Progressing towards a siEVP method circumvented the artifact of dilution often experienced in bulk-analysis methods (Nguyen et al., 2022; Wu et al., 2013). As such, disease-associated proteins and RNAs were preserved in intact siEVPs thus enhancing sensitivities and allowing detection at low concentrations and volumes. The feasibility of analyzing RNAs in siEVPs from the serum of GBM patients unveiled the potential of the ^{siEVP}PRA for liquid biopsy applications. Although the current study focused on GBM vesicular RNA analyses, the ^{siEVP}PRA can easily be adapted to other diseases by customizing the surface chemistry to capture disease-specific epitopes. Furthermore, the multivariate heterogeneity analysis afforded by the ^{siEVP}PRA

can aid in uncovering differences in subpopulation-dependent packaging of biomolecules and illuminate biogenesis pathways. Lastly, the ability for the ^{siEVP}PRA to multiplex across various biomolecular species offers a unique qualitative perspective into siEVP heterogeneity more comprehensively than previously accomplished.

AUTHOR CONTRIBUTIONS

Jingjing Zhang: Conceptualization; data curation; formal analysis; investigation; methodology; visualization; writing—original draft; writing—review & editing. **Xilal Y. Rima**: Conceptualization; data curation; formal analysis; investigation; methodology; software; visualization; writing—original draft; writing—review & editing. **Xinyu Wang**: Data curation; formal analysis; investigation; methodology; software; visualization; writing—original draft; writing—review & editing. **Luong T. H. Nguyen**: Data curation; formal analysis; investigation; methodology. **Kristin Huntoon**: Data curation; formal analysis; investigation; methodology; validation; visualization. **Yifan Ma**: Conceptualization; data curation; formal analysis; investigation; methodology; visualization. **Paola Loreto Palacio**: Data curation; formal analysis; investigation; visualization. **Kim Truc Nguyen**: Data curation; investigation; methodology; visualization. **Karunya Albert**: Data curation; formal analysis; investigation. **Minh-Dao Duong-Thi**: Investigation; methodology. **Nicole Walters**: Investigation; methodology. **Kwang Joo Kwak**: Conceptualization; methodology. **Min Jin Yoon**: Investigation; methodology. **Hong Li**: Conceptualization; methodology. **Jacob Doon-Ralls**: Investigation; methodology. **Colin L. Hisey**: Investigation; writing—review & editing. **Daeyong Lee**: Data curation; investigation. **Yifan Wang**: Data curation; investigation. **Jonghoon Ha**: Data curation; investigation. **Kelsey Scherler**: Data curation; formal analysis; investigation. **Shannon Fallen**: Data curation; formal analysis; investigation. **Inyoul Lee**: Data curation; formal analysis; investigation; supervision. **Andre F. Palmer**: Resources; supervision. **Wen Jiang**: Resources; supervision. **Setty M. Magaña**: Resources; supervision; writing—review & editing. **Kai Wang**: Investigation; project administration; resources; supervision. **Betty Y. S. Kim**: Funding acquisition; project administration; resources; supervision. **L. James Lee**: Funding acquisition; project administration; resources; supervision. **Eduardo Reátegui**: Conceptualization; funding acquisition; methodology; project administration; resources; supervision; writing—original draft; writing—review & editor.

ACKNOWLEDGEMENTS

We acknowledge all cancer patients and healthy volunteers who participated in this study. Electron microscopy was performed at the Center for Electron Microscopy and Analysis (CEMAS) at The Ohio State University. Illustration by Anthony S. Baker, CMI, The Ohio State University. This work was supported by the U.S. National Institutes of Health (NIH) and the National Center for Advancing Translational Sciences (NCATS) under grants UG3/UH3TR002884 (E.R., B.Y.S.K) and U18TR003807 (E.R., L.J.L., K.W., I.L.). Additional support for E.R. was provided by the William G. Lowrie Department of Chemical and Biomolecular Engineering and the Comprehensive Cancer Center at The Ohio State University.

CONFLICT OF INTERESTS

J.Z. and E.R. have filed a provisional patent application for the siEV detection and characterization technology. X.Y.R, K.T.N., and E.R. have filed a provisional patent for siLP-EV detection and characterization technology.

DATA AVAILABILITY STATEMENT

The data supporting the findings of this study are available from the corresponding author upon reasonable request.

ORCID

Xilal Y. Rima https://orcid.org/0000-0001-5633-5887
Luong T. H. Nguyen https://orcid.org/0000-0003-1811-6194
Eduardo Reátegui https://orcid.org/0000-0002-8271-8205

REFERENCES

Abels, E. R., Maas, S. L. N., Nieland, L., Wei, Z., Cheah, P. S., Tai, E., Kolsteeg, C. J., Dusoswa, S. A., Ting, D. T., Hickman, S., El Khoury, J., Krichevsky, A. M., Broekman, M. L. D., & Breakefield, X. O. (2019). Glioblastoma-associated microglia reprogramming is mediated by functional transfer of extracellular miR-21. *Cell Reports*, *28*(12), 3105–3119.e7.

Akers, J. C., Ramakrishnan, V., Kim, R., Skog, J., Nakano, I., Pingle, S., Kalinina, J., Hua, W., Kesari, S., Mao, Y., Breakefield, X. O., Hochberg, F. H., Van Meir, E. G., Carter, B. S., & Chen, C. C. (2013). MiR-21 in the extracellular vesicles (EVs) of cerebrospinal fluid (CSF): A platform for glioblastoma biomarker development. *PLoS ONE*, *8*(10), e78115.

Antonov, J., Goldstein, D. R., Oberli, A., Baltzer, A., Pirotta, M., Fleischmann, A., Altermatt, H. J., & Jaggi, R. (2005). Reliable gene expression measurements from degraded RNA by quantitative real-time PCR depend on short amplicons and a proper normalization. *Laboratory Investigation; A Journal of Technical Methods and Pathology*, *85*(8), 1040–1050.

Arab, T., Mallick, E. R., Huang, Y., Dong, L., Liao, Z., Zhao, Z., Gololobova, O., Smith, B., Haughey, N. J., Pienta, K. J., Slusher, B. S., Tarwater, P. M., Tosar, J. P., Zivkovic, A. M., Vreeland, W. N., Paulaitis, M. E., & Witwer, K. W. (2021). Characterization of extracellular vesicles and synthetic nanoparticles with four orthogonal single-particle analysis platforms. *Journal of Extracellular Vesicles*, *10*(6), e12079.

Batagov, A. O., & Kurochkin, I. V. (2013). Exosomes secreted by human cells transport largely mRNA fragments that are enriched in the 3'-untranslated regions. *Biology Direct*, *8*, 12.

Bonté, F., & Juliano, R. L. (1986). Interactions of liposomes with serum proteins. *Chemistry and Physics of Lipids*, *40*(2–4), 359–372.

Breitwieser, K., Koch, L. F., Tertel, T., Proestler, E., Burgers, L. D., Lipps, C., Adjaye, J., Fürst, R., Giebel, B., & Saul, M. J. (2022). Detailed Characterization of small extracellular vesicles from different cell types based on tetraspanin composition by ExoView R100 platform. *International Journal of Molecular Sciences*, *23*(15), 8544.

Brennan, K., Martin, K., FitzGerald, S. P., O'Sullivan, J., Wu, Y., Blanco, A., Richardson, C., & Mc Gee, M. M. (2020). A comparison of methods for the isolation and separation of extracellular vesicles from protein and lipid particles in human serum. *Scientific Reports*, *10*(1), 1039.

Burstein, M., Scholnick, H. R., & Morfin, R. (1970). Rapid method for the isolation of lipoproteins from human serum by precipitation with polyanions. *Journal of Lipid Research*, *11*(6), 583–595.

Busatto, S., Yang, Y., Iannotta, D., Davidovich, I., Talmon, Y., & Wolfram, J. (2022). Considerations for extracellular vesicle and lipoprotein interactions in cell culture assays. *Journal of Extracellular Vesicles*, *11*(4), e12202.

Busatto, S., Yang, Y., Walker, S. A., Davidovich, I., Lin, W. H., Lewis-Tuffin, L., Anastasiadis, P. Z., Sarkaria, J., Talmon, Y., Wurtz, G., & Wolfram, J. (2020). Brain metastases-derived extracellular vesicles induce binding and aggregation of low-density lipoprotein. *Journal of Nanobiotechnology*, *18*(1), 162.

Buschow, S. I., Nolte-'t Hoen, E. N., van Niel, G., Pols, M. S., ten Broeke, T., Lauwen, M., Ossendorp, F., Melief, C. J., Raposo, G., Wubbolts, R., Wauben, M. H., & Stoorvogel, W. (2009). MHC II in dendritic cells is targeted to lysosomes or T cell-induced exosomes via distinct multivesicular body pathways. *Traffic (Copenhagen, Denmark)*, *10*(10), 1528–1542.

Chairoungdua, A., Smith, D. L., Pochard, P., Hull, M., & Caplan, M. J. (2010). Exosome release of β-catenin: A novel mechanism that antagonizes Wnt signaling. *The Journal of Cell Biology*, *190*(6), 1079–1091.

Chattopadhyay, P. K., Price, D. A., Harper, T. F., Betts, M. R., Yu, J., Gostick, E., Perfetto, S. P., Goepfert, P., Koup, R. A., De Rosa, S. C., Bruchez, M. P., & Roederer, M. (2006). Quantum dot semiconductor nanocrystals for immunophenotyping by polychromatic flow cytometry. *Nature Medicine*, *12*(8), 972–977.

Chen, K. H., Boettiger, A. N., Moffitt, J. R., Wang, S., & Zhuang, X. (2015). RNA imaging. Spatially resolved, highly multiplexed RNA profiling in single cells. *Science (New York, N.Y.)*, *348*(6233), aaa6090.

Chen, Y., Zeng, C., Zhan, Y., Wang, H., Jiang, X., & Li, W. (2017). Aberrant low expression of p85α in stromal fibroblasts promotes breast cancer cell metastasis through exosome-mediated paracrine Wnt10b. *Oncogene*, *36*(33), 4692–4705.

Clancy, J. W., Zhang, Y., Sheehan, C., & D'Souza-Schorey, C. (2019). An ARF6-Exportin-5 axis delivers pre-miRNA cargo to tumour microvesicles. *Nature Cell Biology*, *21*(7), 856–866.

Conigliaro, A., & Cicchini, C. (2018). Exosome-mediated signaling in epithelial to mesenchymal transition and tumor progression. *Journal of Clinical Medicine*, *8*(1), 26.

Crouser, E. D., Julian, M. W., Bicer, S., Ghai, V., Kim, T. K., Maier, L. A., Gillespie, M., Hamzeh, N. Y., & Wang, K. (2021). Circulating exosomal microRNA expression patterns distinguish cardiac sarcoidosis from myocardial ischemia. *PLoS ONE*, *16*(1), e0246083.

Daaboul, G. G., Gagni, P., Benussi, L., Bettotti, P., Ciani, M., Cretich, M., Freedman, D. S., Ghidoni, R., Ozkumur, A. Y., Piotto, C., Prosperi, D., Santini, B., Ünlü, M. S., & Chiari, M. (2016). Digital detection of exosomes by interferometric imaging. *Scientific Reports*, *6*, 37246.

Daaboul, G. G., Yurt, A., Zhang, X., Hwang, G. M., Goldberg, B. B., & Ünlü, M. S. (2010). High-throughput detection and sizing of individual low-index nanoparticles and viruses for pathogen identification. *Nano Letters*, *10*(11), 4727–4731.

Dellar, E. R., Hill, C., Melling, G. E., Carter, D. R. F., & Baena-Lopez, L. A. (2022). Unpacking extracellular vesicles: RNA cargo loading and function. *Journal of Extracellular Biology*, *1*, e40.

Dellar, E. R., Hill, C., Melling, G. E., Carter, D. R. F., & Baena-Lopez, L. A. (2022). Unpacking extracellular vesicles: RNA cargo loading and function. *Journal of Extracellular Biology*, *1*, e40.

Deng, F., Ratri, A., Deighan, C., Daaboul, G., Geiger, P. C., & Christenson, L. K. (2022). Single-particle interferometric reflectance imaging characterization of individual extracellular vesicles and population dynamics. *Journal of Visualized Experiments: JoVE*, *179*, e62988.

de Voogt, W. S., Tanenbaum, M. E., & Vader, P. (2021). Illuminating RNA trafficking and functional delivery by extracellular vesicles. *Advanced Drug Delivery Reviews*, *174*, 250–264.

Erdbrügger, U., & Lannigan, J. (2016). Analytical challenges of extracellular vesicle detection: A comparison of different techniques. *Cytometry. Part A: the journal of the International Society for Analytical Cytology*, *89*(2), 123–134.

Escola, J. M., Kleijmeer, M. J., Stoorvogel, W., Griffith, J. M., Yoshie, O., & Geuze, H. J. (1998). Selective enrichment of tetraspan proteins on the internal vesicles of multivesicular endosomes and on exosomes secreted by human B-lymphocytes. *The Journal of Biological Chemistry*, *273*(32), 20121–20127.

Etheridge, A., Wang, K., Baxter, D., & Galas, D. (2018). Preparation of small RNA NGS libraries from biofluids. *Methods in Molecular Biology (Clifton, N.J.)*, *1740*, 163–175.

Fallen, S., Baxter, D., Wu, X., Kim, T. K., Shynlova, O., Lee, M. Y., Scherler, K., Lye, S., Hood, L., & Wang, K. (2018). Extracellular vesicle RNAs reflect placenta dysfunction and are a biomarker source for preterm labour. *Journal of Cellular and Molecular Medicine*, *22*(5), 2760–2773.

Filipazzi, P., Bürdek, M., Villa, A., Rivoltini, L., & Huber, V. (2012). Recent advances on the role of tumor exosomes in immunosuppression and disease progression. *Seminars in Cancer Biology*, *22*(4), 342–349.

Gatto, L., Franceschi, E., Di Nunno, V., Tosoni, A., Lodi, R., & Brandes, A. A. (2021). Liquid biopsy in glioblastoma management: From current research to future perspectives. *The Oncologist*, *26*(10), 865–878.

Ghai, V., Wu, X., Bheda-Malge, A., Argyropoulos, C. P., Bernardo, J. F., Orchard, T., Galas, D., & Wang, K. (2017). Genome-wide profiling of urinary extracellular vesicle microRNAs associated with diabetic nephropathy in type 1 diabetes. *Kidney International Reports*, *3*(3), 555–572.

Giraldez, M. D., Spengler, R. M., Etheridge, A., Godoy, P. M., Barczak, A. J., Srinivasan, S., De Hoff, P. L., Tanriverdi, K., Courtright, A., Lu, S., Khoory, J., Rubio, R., Baxter, D., Driedonks, T. A. P., Buermans, H. P. J., Nolte-'t Hoen, E. N. M., Jiang, H., Wang, K., Ghiran, I., … Tewari, M. (2018). Comprehensive multi-center assessment of small RNA-seq methods for quantitative miRNA profiling. *Nature Biotechnology*, *36*(8), 746–757.

Han, C., Kang, H., Yi, J., Kang, M., Lee, H., Kwon, Y., Jung, J., Lee, J., & Park, J. (2021). Single-vesicle imaging and co-localization analysis for tetraspanin profiling of individual extracellular vesicles. *Journal of Extracellular Vesicles*, *10*(3), e12047.

Hilton, S. H., & White, I. M. (2021). Advances in the analysis of single extracellular vesicles: A critical review. *Sensors and Actuators Reports*, *3*, 100052.

Hinger, S. A., Cha, D. J., Franklin, J. L., Higginbotham, J. N., Dou, Y., Ping, J., Shu, L., Prasad, N., Levy, S., Zhang, B., Liu, Q., Weaver, A. M., Coffey, R. J., & Patton, J. G. (2018). Diverse long RNAs are differentially sorted into extracellular vesicles secreted by colorectal cancer cells. *Cell Reports*, *25*(3), 715–725.e4.

Hoshino, A., Costa-Silva, B., Shen, T. L., Rodrigues, G., Hashimoto, A., Tesic Mark, M., Molina, H., Kohsaka, S., Di Giannatale, A., Ceder, S., Singh, S., Williams, C., Soplop, N., Uryu, K., Pharmer, L., King, T., Bojmar, L., Davies, A. E., Ararso, Y., … Lyden, D. (2015). Tumour exosome integrins determine organotropic metastasis. *Nature*, *527*(7578), 329–335.

Hu, J., Sheng, Y., Kwak, K. J., Shi, J., Yu, B., & Lee, L. J. (2017). A signal-amplifiable biochip quantifies extracellular vesicle-associated RNAs for early cancer detection. *Nature Communications*, *8*(1), 1683.

Hutterer, M., Knyazev, P., Abate, A., Reschke, M., Maier, H., Stefanova, N., Knyazeva, T., Barbieri, V., Reindl, M., Muigg, A., Kostron, H., Stockhammer, G., & Ullrich, A. (2008). Axl and growth arrest-specific gene 6 are frequently overexpressed in human gliomas and predict poor prognosis in patients with glioblastoma multiforme. *Clinical Cancer Research: An Official Journal of the American Association for Cancer Research*, *14*(1), 130–138.

Im, H., Shao, H., Park, Y. I., Peterson, V. M., Castro, C. M., Weissleder, R., & Lee, H. (2014). Label-free detection and molecular profiling of exosomes with a nano-plasmonic sensor. *Nature Biotechnology*, *32*(5), 490–495.

Jeppesen, D. K., Fenix, A. M., Franklin, J. L., Higginbotham, J. N., Zhang, Q., Zimmerman, L. J., Liebler, D. C., Ping, J., Liu, Q., Evans, R., Fissell, W. H., Patton, J. G., Rome, L. H., Burnette, D. T., & Coffey, R. J. (2019). Reassessment of exosome composition. *Cell*, *177*(2), 428–445.e18.

Kalluri, R., & LeBleu, V. S. (2020). The biology, function, and biomedical applications of exosomes. *Science (New York, N.Y.)*, *367*(6478), eaau6977.

Karttunen, J., Heiskanen, M., Navarro-Ferrandis, V., Das Gupta, S., Lipponen, A., Puhakka, N., Rilla, K., Koistinen, A., & Pitkänen, A. (2018). Precipitation-based extracellular vesicle isolation from rat plasma co-precipitate vesicle-free microRNAs. *Journal of Extracellular Vesicles*, *8*(1), 1555410.

Koster, H. J., Rojalin, T., Powell, A., Pham, D., Mizenko, R. R., Birkeland, A. C., & Carney, R. P. (2021). Surface enhanced Raman scattering of extracellular vesicles for cancer diagnostics despite isolation dependent lipoprotein contamination. *Nanoscale*, *13*(35), 14760–14776.

Kowal, J., Arras, G., Colombo, M., Jouve, M., Morath, J. P., Primdal-Bengtson, B., Dingli, F., Loew, D., Tkach, M., & Théry, C. (2016). Proteomic comparison defines novel markers to characterize heterogeneous populations of extracellular vesicle subtypes. *Proceedings of the National Academy of Sciences of the United States of America*, *113*(8), E968–E977.

Kumar, S., Maniya, N., Wang, C., Senapati, S., & Chang, H. C. (2023). Quantifying PON1 on HDL with nanoparticle-gated electrokinetic membrane sensor for accurate cardiovascular risk assessment. *Nature Communications*, *14*(1), 557.

Kwon, Y., & Park, J. (2022). Methods to analyze extracellular vesicles at single particle level. *Micro and Nano Systems*, *10*, 14.

Lee, K., Fraser, K., Ghaddar, B., Yang, K., Kim, E., Balaj, L., Chiocca, E. A., Breakefield, X. O., Lee, H., & Weissleder, R. (2018). Multiplexed profiling of single extracellular vesicles. *ACS Nano*, *12*(1), 494–503.

Lennon, K. M., Wakefield, D. L., Maddox, A. L., Brehove, M. S., Willner, A. N., Garcia-Mansfield, K., Meechoovet, B., Reiman, R., Hutchins, E., Miller, M. M., Goel, A., Pirrotte, P., Van Keuren-Jensen, K., & Jovanovic-Talisman, T. (2019). Single molecule characterization of individual extracellular vesicles from pancreatic cancer. *Journal of Extracellular Vesicles*, *8*(1), 1685634.

Lou, W., Ding, B., Xu, L., & Fan, W. (2019). Construction of potential glioblastoma multiforme-related miRNA-mRNA regulatory network. *Frontiers in Molecular Neuroscience*, *12*, 66.

Mackness, M. I., Arrol, S., & Durrington, P. N. (1991). Paraoxonase prevents accumulation of lipoperoxides in low-density lipoprotein. *FEBS Letters*, *286*(1–2), 152–154.

Madadi, S., & Soleimani, M. (2019). Comparison of miR-16 and cel-miR-39 as reference controls for serum miRNA normalization in colorectal cancer. *Journal of Cellular Biochemistry*, *120*(4), 4802–4803.

Marzolf, B., & Troisch, P. (2006). SLIMarray: Lightweight software for microarray facility management. *Source Code for Biology and Medicine*, *1*, 5.

Mateescu, B., Kowal, E. J., van Balkom, B. W., Bartel, S., Bhattacharyya, S. N., Buzás, E. I., Buck, A. H., de Candia, P., Chow, F. W., Das, S., Driedonks, T. A., Fernández-Messina, L., Haderk, F., Hill, A. F., Jones, J. C., Van Keuren-Jensen, K. R., Lai, C. P., Lässer, C., Liegro, I. D., … Nolte-'t Hoen, E. N. (2017). Obstacles and opportunities in the functional analysis of extracellular vesicle RNA—An ISEV position paper. *Journal of Extracellular Vesicles*, *6*(1), 1286095.

Mathieu, M., Névo, N., Jouve, M., Valenzuela, J. I., Maurin, M., Verweij, F. J., Palmulli, R., Lankar, D., Dingli, F., Loew, D., Rubinstein, E., Boncompain, G., Perez, F., & Théry, C. (2021). Specificities of exosome versus small ectosome secretion revealed by live intracellular tracking of CD63 and CD9. *Nature Communications*, *12*(1), 4389.

McGillicuddy, L. T., Fromm, J. A., Hollstein, P. E., Kubek, S., Beroukhim, R., De Raedt, T., Johnson, B. W., Williams, S. M., Nghiemphu, P., Liau, L. M., Cloughesy, T. F., Mischel, P. S., Parret, A., Seiler, J., Moldenhauer, G., Scheffzek, K., Stemmer-Rachamimov, A. O., Sawyers, C. L., Brennan, C., … Cichowski, K. (2009). Proteasomal and genetic inactivation of the NF1 tumor suppressor in gliomagenesis. *Cancer Cell*, *16*(1), 44–54.

McNamara, R. P., Zhou, Y., Eason, A. B., Landis, J. T., Chambers, M. G., Willcox, S., Peterson, T. A., Schouest, B., Maness, N. J., MacLean, A. G., Costantini, L. M., Griffith, J. D., & Dittmer, D. P. (2022). Imaging of surface microdomains on individual extracellular vesicles in 3-D. *Journal of Extracellular Vesicles*, *11*(3), e12191.

Mitchell, P. S., Parkin, R. K., Kroh, E. M., Fritz, B. R., Wyman, S. K., Pogosova-Agadjanyan, E. L., Peterson, A., Noteboom, J., O'Briant, K. C., Allen, A., Lin, D. W., Urban, N., Drescher, C. W., Knudsen, B. S., Stirewalt, D. L., Gentleman, R., Vessella, R. L., Nelson, P. S., Martin, D. B., & Tewari, M. (2008). Circulating microRNAs as stable blood-based markers for cancer detection. *Proceedings of the National Academy of Sciences of the United States of America*, *105*(30), 10513–10518.

Mizenko, R. R., Brostoff, T., Rojalin, T., Koster, H. J., Swindell, H. S., Leiserowitz, G. S., Wang, A., & Carney, R. P. (2021). Tetraspanins are unevenly distributed across single extracellular vesicles and bias sensitivity to multiplexed cancer biomarkers. *Journal of Nanobiotechnology*, *19*(1), 250.

Momen-Heravi, F., Balaj, L., Alian, S., Mantel, P. Y., Halleck, A. E., Trachtenberg, A. J., Soria, C. E., Oquin, S., Bonebreak, C. M., Saracoglu, E., Skog, J., & Kuo, W. P. (2013). Current methods for the isolation of extracellular vesicles. *Biological Chemistry*, *394*(10), 1253–1262.

Muralidharan-Chari, V., Clancy, J., Plou, C., Romao, M., Chavrier, P., Raposo, G., & D'Souza-Schorey, C. (2009). ARF6-regulated shedding of tumor cell-derived plasma membrane microvesicles. *Current Biology: CB*, *19*(22), 1875–1885.

Nguyen, L. T. H., Zhang, J., Rima, X. Y., Wang, X., Kwak, K. J., Okimoto, T., Amann, J., Yoon, M. J., Shukuya, T., Chiang, C. L., Walters, N., Ma, Y., Belcher, D., Li, H., Palmer, A. F., Carbone, D. P., Lee, L. J., & Reátegui, E. (2022). An immunogold single extracellular vesicular RNA and protein (^{Au} SERP) biochip to predict responses to immunotherapy in non-small cell lung cancer patients. *Journal of Extracellular Vesicles*, *11*(9), e12258.

Noble, J. M., Roberts, L. M., Vidavsky, N., Chiou, A. E., Fischbach, C., Paszek, M. J., Estroff, L. A., & Kourkoutis, L. F. (2020). Direct comparison of optical and electron microscopy methods for structural characterization of extracellular vesicles. *Journal of Structural Biology*, *210*(1), 107474.

Panagopoulou, M. S., Wark, A. W., Birch, D. J. S., & Gregory, C. D. (2020). Phenotypic analysis of extracellular vesicles: A review on the applications of fluorescence. *Journal of Extracellular Vesicles*, *9*(1), 1710020.

Pascucci, L., & Scattini, G. (2021). Imaging extracelluar vesicles by transmission electron microscopy: Coping with technical hurdles and morphological interpretation. *Biochimica et Biophysica Acta. General Subjects*, *1865*(4), 129648.

Piontek, M. C., & Roos, W. H. (2022). Lipoprotein particles exhibit distinct mechanical properties. *Jpurnal of Extracellular Biology*, *1*, e68.

Prachayasittikul, V., Isarankura-Na-Ayudhya, C., Tantimongcolwat, T., Nantasenamat, C., & Galla, H. J. (2007). EDTA-induced membrane fluidization and destabilization: Biophysical studies on artificial lipid membranes. *Acta Biochimica et Biophysica Sinica*, *39*(11), 901–913.

Qiu, L., Liu, X., Zhu, L., Luo, L., Sun, N., & Pei, R. (2023). Current advances in technologies for single extracellular vesicle analysis and its clinical applications in cancer diagnosis. *Biosensors*, *13*(1), 129.

Qiu, W., Guo, X., Li, B., Wang, J., Qi, Y., Chen, Z., Zhao, R., Deng, L., Qian, M., Wang, S., Zhang, Z., Guo, Q., Zhang, S., Pan, Z., Zhao, S., Xue, H., & Li, G. (2021). Exosomal miR-1246 from glioma patient body fluids drives the differentiation and activation of myeloid-derived suppressor cells. *Molecular Therapy: The Journal of the American Society of Gene Therapy*, *29*(12), 3449–3464.

Ramirez, M. I., Amorim, M. G., Gadelha, C., Milic, I., Welsh, J. A., Freitas, V. M., Nawaz, M., Akbar, N., Couch, Y., Makin, L., Cooke, F., Vettore, A. L., Batista, P. X., Freezor, R., Pezuk, J. A., Rosa-Fernandes, L., Carreira, A. C. O., Devitt, A., Jacobs, L., … Dias-Neto, E. (2018). Technical challenges of working with extracellular vesicles. *Nanoscale*, *10*(3), 881–906.

Reátegui, E., van der Vos, K. E., Lai, C. P., Zeinali, M., Atai, N. A., Aldikacti, B., Floyd, F. P. Jr, Khankhel, A. H., Thapar, V., Hochberg, F. H., Sequist, L. V., Nahed, B. V., Carter, B. S., Toner, M., Balaj, L., Ting, D. T., Breakefield, X. O., & Stott, S. L. (2018). Engineered nanointerfaces for microfluidic isolation and molecular profiling of tumor-specific extracellular vesicles. *Nature Communications*, *9*(1), 175.

Ridolfi, A., Brucale, M., Montis, C., Caselli, L., Paolini, L., Borup, A., Boysen, A. T., Loria, F., van Herwijnen, M. J. C., Kleinjan, M., Nejsum, P., Zarovni, N., Wauben, M. H. M., Berti, D., Bergese, P., & Valle, F. (2020). AFM-based high-throughput nanomechanical screening of single extracellular vesicles. *Analytical Chemistry*, *92*(15), 10274–10282.

Rikkert, L. G., Nieuwland, R., Terstappen, L. W. M. M., & Coumans, F. A. W. (2019). Quality of extracellular vesicle images by transmission electron microscopy is operator and protocol dependent. *Journal of Extracellular Vesicles*, *8*(1), 1555419.

Rima, X. Y., Zhang, J., Nguyen, L. T. H., Rajasuriyar, A., Yoon, M. J., Chiang, C. L., Walters, N., Kwak, K. J., Lee, L. J., & Reátegui, E. (2022). Microfluidic harvesting of breast cancer tumor spheroid-derived extracellular vesicles from immobilized microgels for single-vesicle analysis. *Lab on a Chip*, *22*(13), 2502–2518.

Rodrigues, G., Hoshino, A., Kenific, C. M., Matei, I. R., Steiner, L., Freitas, D., Kim, H. S., Oxley, P. R., Scandariato, I., Casanova-Salas, I., Dai, J., Badwe, C. R., Gril, B., Tešić Mark, M., Dill, B. D., Molina, H., Zhang, H., Benito-Martin, A., Bojmar, L., … Lyden, D. (2019). Tumour exosomal CEMIP protein promotes cancer cell colonization in brain metastasis. *Nature Cell Biology*, *21*(11), 1403–1412.

Rogers, M. A., Buffolo, F., Schlotter, F., Atkins, S. K., Lee, L. H., Halu, A., Blaser, M. C., Tsolaki, E., Higashi, H., Luther, K., Daaboul, G., Bouten, C. V. C., Body, S. C., Singh, S. A., Bertazzo, S., Libby, P., Aikawa, M., & Aikawa, E. (2020). Annexin A1-dependent tethering promotes extracellular vesicle aggregation revealed with single-extracellular vesicle analysis. *Science Advances*, *6*(38), eabb1244.

Royo, F., Zuñiga-Garcia, P., Sanchez-Mosquera, P., Egia, A., Perez, A., Loizaga, A., Arceo, R., Lacasa, I., Rabade, A., Arrieta, E., Bilbao, R., Unda, M., Carracedo, A., & Falcon-Perez, J. M. (2016). Different EV enrichment methods suitable for clinical settings yield different subpopulations of urinary extracellular vesicles from human samples. *Journal of Extracellular Vesicles*, *5*, 29497.

Sadahiro, H., Kang, K. D., Gibson, J. T., Minata, M., Yu, H., Shi, J., Chhipa, R., Chen, Z., Lu, S., Simoni, Y., Furuta, T., Sabit, H., Zhang, S., Bastola, S., Yamaguchi, S., Alsheikh, H., Komarova, S., Wang, J., Kim, S. H., … Nakano, I. (2018). Activation of the receptor tyrosine kinase AXL regulates the immune microenvironment in glioblastoma. *Cancer Research*, *78*(11), 3002–3013.

Saftics, A., Abuelreich, S., Romano, E., Ghaeli, I., Jiang, N., Spanos, M., Lennon, K. M., Singh, G., Das, S., Van Keuren-Jensen, K., & Jovanovic-Talisman, T. (2023). Single extracellular VEsicle nanoscopy. *Journal of Extracellular Vesicles*, *12*(7), e12346.

Salmond, N., Khanna, K., Owen, G. R., & Williams, K. C. (2021). Nanoscale flow cytometry for immunophenotyping and quantitating extracellular vesicles in blood plasma. *Nanoscale*, *13*(3), 2012–2025.

Santos, J. C., Lima, N. D. S., Sarian, L. O., Matheu, A., Ribeiro, M. L., & Derchain, S. F. M. (2018). Exosome-mediated breast cancer chemoresistance via miR-155 transfer. *Scientific Reports*, *8*(1), 829.

Simonsen, J. B. (2017). What are we looking at? Extracellular vesicles, lipoproteins, or both? *Circulation Research*, *121*(8), 920–922.

Sódar, B. W., Kittel, Á., Pálóczi, K., Vukman, K. V., Osteikoetxea, X., Szabó-Taylor, K., Németh, A., Sperlágh, B., Baranyai, T., Giricz, Z., Wiener, Z., Turiák, L., Drahos, L., Pállinger, É., Vékey, K., Ferdinandy, P., Falus, A., & Buzás, E. I. (2016). Low-density lipoprotein mimics blood plasma-derived exosomes and microvesicles during isolation and detection. *Scientific Reports*, *6*, 24316.

Spitzberg, J. D., Ferguson, S., Yang, K. S., Peterson, H. M., Carlson, J. C. T., & Weissleder, R. (2023). Multiplexed analysis of EV reveals specific biomarker composition with diagnostic impact. *Nature Communications*, *14*(1), 1239.

Stauffer, W., Sheng, H., & Lim, H. N. (2018). EzColocalization: An ImageJ plugin for visualizing and measuring colocalization in cells and organisms. *Scientific Reports*, *8*(1), 15764.

Strale, P. O., Azioune, A., Bugnicourt, G., Lecomte, Y., Chahid, M., & Studer, V. (2016). Multiprotein printing by light-induced molecular adsorption. *Advanced Materials (Deerfield Beach, Fla.)*, *28*(10), 2024–2029.

Su, Z., Kishida, S., Tsubota, S., Sakamoto, K., Cao, D., Kiyonari, S., Ohira, M., Kamijo, T., Narita, A., Xu, Y., Takahashi, Y., & Kadomatsu, K. (2017). Neurocan, an extracellular chondroitin sulfate proteoglycan, stimulates neuroblastoma cells to promote malignant phenotypes. *Oncotarget*, *8*(63), 106296–106310.

Thane, K. E., Davis, A. M., & Hoffman, A. M. (2019). Improved methods for fluorescent labeling and detection of single extracellular vesicles using nanoparticle tracking analysis. *Scientific Reports*, *9*(1), 12295.

Théry, C., Regnault, A., Garin, J., Wolfers, J., Zitvogel, L., Ricciardi-Castagnoli, P., Raposo, G., & Amigorena, S. (1999). Molecular characterization of dendritic cell-derived exosomes. Selective accumulation of the heat shock protein hsc73. *The Journal of Cell Biology*, *147*(3), 599–610.

Tian, Y., Gong, M., Hu, Y., Liu, H., Zhang, W., Zhang, M., Hu, X., Aubert, D., Zhu, S., Wu, L., & Yan, X. (2019). Quality and efficiency assessment of six extracellular vesicle isolation methods by nano-flow cytometry. *Journal of Extracellular Vesicles*, *9*(1), 1697028.

Tominaga, N., Kosaka, N., Ono, M., Katsuda, T., Yoshioka, Y., Tamura, K., Lötvall, J., Nakagama, H., & Ochiya, T. (2015). Brain metastatic cancer cells release microRNA-181c-containing extracellular vesicles capable of destructing blood-brain barrier. *Nature Communications*, *6*, 6716.

Tóth, E. Á., Turiák, L., Visnovitz, T., Cserép, C., Mázló, A., Sódar, B. W., Försönits, A. I., Petővári, G., Sebestyén, A., Komlósi, Z., Drahos, L., Kittel, Á., Nagy, G., Bácsi, A., Dénes, Á., Gho, Y. S., Szabó-Taylor, K. É., & Buzás, E. I. (2021). Formation of a protein corona on the surface of extracellular vesicles in blood plasma. *Journal of Extracellular Vesicles*, *10*(11), e12140.

Vaara, M. (1992). Agents that increase the permeability of the outer membrane. *Microbiological Reviews*, *56*(3), 395–411.

Valm, A. M., Oldenbourg, R., & Borisy, G. G. (2016). Multiplexed spectral imaging of 120 different fluorescent labels. *PLoS One*, *11*(7), e0158495.

van der Pol, E., Coumans, F. A., Grootemaat, A. E., Gardiner, C., Sargent, I. L., Harrison, P., Sturk, A., van Leeuwen, T. G., & Nieuwland, R. (2014). Particle size distribution of exosomes and microvesicles determined by transmission electron microscopy, flow cytometry, nanoparticle tracking analysis, and resistive pulse sensing. *Journal of Thrombosis and Haemostasis: JTH*, *12*(7), 1182–1192.

Van Deun, J., Mestdagh, P., Sormunen, R., Cocquyt, V., Vermaelen, K., Vandesompele, J., Bracke, M., De Wever, O., & Hendrix, A. (2014). The impact of disparate isolation methods for extracellular vesicles on downstream RNA profiling. *Journal of Extracellular Vesicles*, *3*, 24858.

van Niel, G., Charrin, S., Simoes, S., Romao, M., Rochin, L., Saftig, P., Marks, M. S., Rubinstein, E., & Raposo, G. (2011). The tetraspanin CD63 regulates ESCRT-independent and -dependent endosomal sorting during melanogenesis. *Developmental Cell*, *21*(4), 708–721.

Vickers, K. C., Palmisano, B. T., Shoucri, B. M., Shamburek, R. D., & Remaley, A. T. (2011). MicroRNAs are transported in plasma and delivered to recipient cells by high-density lipoproteins. *Nature Cell Biology*, *13*(4), 423–433.

Vigneron, N., Meryet-Figuière, M., Guttin, A., Issartel, J. P., Lambert, B., Briand, M., Louis, M. H., Vernon, M., Lebailly, P., Lecluse, Y., Joly, F., Krieger, S., Lheureux, S., Clarisse, B., Leconte, A., Gauduchon, P., Poulain, L., & Denoyelle, C. (2016). Towards a new standardized method for circulating miRNAs profiling in clinical studies: Interest of the exogenous normalization to improve miRNA signature accuracy. *Molecular Oncology*, *10*(7), 981–992.

Vogel, R., Savage, J., Muzard, J., Camera, G. D., Vella, G., Law, A., Marchioni, M., Mehn, D., Geiss, O., Peacock, B., Aubert, D., Calzolai, L., Caputo, F., & Prina-Mello, A. (2021). Measuring particle concentration of multimodal synthetic reference materials and extracellular vesicles with orthogonal techniques: Who is up to the challenge? *Journal of Extracellular Vesicles*, *10*(3), e12052.

Wang, N., Zheng, J., Chen, Z., Liu, Y., Dura, B., Kwak, M., Xavier-Ferrucio, J., Lu, Y. C., Zhang, M., Roden, C., Cheng, J., Krause, D. S., Ding, Y., Fan, R., & Lu, J. (2019). Single-cell microRNA-mRNA co-sequencing reveals non-genetic heterogeneity and mechanisms of microRNA regulation. *Nature Communications*, *10*(1), 95.

Wei, Z., Batagov, A. O., Schinelli, S., Wang, J., Wang, Y., El Fatimy, R., Rabinovsky, R., Balaj, L., Chen, C. C., Hochberg, F., Carter, B., Breakefield, X. O., & Krichevsky, A. M. (2017). Coding and noncoding landscape of extracellular RNA released by human glioma stem cells. *Nature Communications*, *8*(1), 1145.

Westphal, M., & Lamszus, K. (2015). Circulating biomarkers for gliomas. *Nature Reviews. Neurology*, *11*(10), 556–566.

Wolf, M., Poupardin, R. W., Ebner-Peking, P., Andrade, A. C., Blöchl, C., Obermayer, A., Gomes, F. G., Vari, B., Maeding, N., Eminger, E., Binder, H. M., Raninger, A. M., Hochmann, S., Brachtl, G., Spittler, A., Heuser, T., Ofir, R., Huber, C. G., Aberman, Z., … Strunk, D. (2022). A functional corona around extracellular vesicles enhances angiogenesis, skin regeneration and immunomodulation. *Journal of Extracellular Vesicles*, *11*(4), e12207.

Wolf, M., Poupardin, R. W., Ebner-Peking, P., Andrade, A. C., Blöchl, C., Obermayer, A., Gomes, F. G., Vari, B., Maeding, N., Eminger, E., Binder, H. M., Raninger, A. M., Hochmann, S., Brachtl, G., Spittler, A., Heuser, T., Ofir, R., Huber, C. G., Aberman, Z., … Strunk, D. (2022). A functional corona around extracellular vesicles enhances angiogenesis, skin regeneration and immunomodulation. *Journal of Extracellular Vesicles*, *11*(4), e12207.

Wu, D., Yan, J., Shen, X., Sun, Y., Thulin, M., Cai, Y., Wik, L., Shen, Q., Oelrich, J., Qian, X., Dubois, K. L., Ronquist, K. G., Nilsson, M., Landegren, U., & Kamali-Moghaddam, M. (2019). Profiling surface proteins on individual exosomes using a proximity barcoding assay. *Nature Communications*, *10*(1), 3854.

Wu, X., Kim, T. K., Baxter, D., Scherler, K., Gordon, A., Fong, O., Etheridge, A., Galas, D. J., & Wang, K. (2017). sRNAnalyzer-a flexible and customizable small RNA sequencing data analysis pipeline. *Nucleic Acids Research*, *45*(21), 12140–12151.

Wu, Y., Kwak, K. J., Agarwal, K., Marras, A., Wang, C., Mao, Y., Huang, X., Ma, J., Yu, B., Lee, R., Vachani, A., Marcucci, G., Byrd, J. C., Muthusamy, N., Otterson, G., Huang, K., Castro, C. E., Paulaitis, M., Nana-Sinkam, S. P., & Lee, L. J. (2013). Detection of extracellular RNAs in cancer and viral infection via tethered cationic lipoplex nanoparticles containing molecular beacons. *Analytical Chemistry*, *85*(23), 11265–11274.

Yáñez-Mó, M., Siljander, P. R., Andreu, Z., Zavec, A. B., Borràs, F. E., Buzas, E. I., Buzas, K., Casal, E., Cappello, F., Carvalho, J., Colás, E., Cordeiro-da Silva, A., Fais, S., Falcon-Perez, J. M., Ghobrial, I. M., Giebel, B., Gimona, M., Graner, M., Gursel, I., … De Wever, O. (2015). Biological properties of extracellular vesicles and their physiological functions. *Journal of Extracellular Vesicles*, *4*, 27066.

Yang, Y., Shen, G., Wang, H., Li, H., Zhang, T., Tao, N., Ding, X., & Yu, H. (2018). Interferometric plasmonic imaging and detection of single exosomes. *Proceedings of the National Academy of Sciences of the United States of America*, *115*(41), 10275–10280.

Yang, Z., Shi, J., Xie, J., Wang, Y., Sun, J., Liu, T., Zhao, Y., Zhao, X., Wang, X., Ma, Y., Malkoc, V., Chiang, C., Deng, W., Chen, Y., Fu, Y., Kwak, K. J., Fan, Y., Kang, C., Yin, C., … Lee, L. J. (2020). Large-scale generation of functional mRNA-encapsulating exosomes via cellular nanoporation. *Nature Biomedical Engineering*, *4*(1), 69–83.

Yekula, A., Yekula, A., Muralidharan, K., Kang, K., Carter, B. S., & Balaj, L. (2020). Extracellular Vesicles in Glioblastoma Tumor Microenvironment. *Frontiers in Immunology*, *10*, 3137.

Yuana, Y., Levels, J., Grootemaat, A., Sturk, A., & Nieuwland, R. (2014). Co-isolation of extracellular vesicles and high-density lipoproteins using density gradient ultracentrifugation. *Journal of Extracellular Vesicles*, *3*, 23262.

Yurtsever, A., Yoshida, T., Behjat, A. B., Araki, Y., Hanayama, R., & Fukuma, T. (2021). Structural and mechanical characteristics of exosomes from osteosarcoma cells explored by 3D-atomic force microscopy. *Nanoscale*, *13*(13), 6661–6677.

Zand Karimi, H., Baldrich, P., Rutter, B. D., Borniego, L., Zajt, K. K., Meyers, B. C., & Innes, R. W. (2022). Arabidopsis apoplastic fluid contains sRNA- and circular RNA-protein complexes that are located outside extracellular vesicles. *The Plant Cell*, *34*(5), 1863–1881.

Zeng, A. L., Yan, W., Liu, Y. W., Wang, Z., Hu, Q., Nie, E., Zhou, X., Li, R., Wang, X. F., Jiang, T., & You, Y. P. (2017). Tumour exosomes from cells harbouring PTPRZ1-MET fusion contribute to a malignant phenotype and temozolomide chemoresistance in glioblastoma. *Oncogene*, *36*(38), 5369–5381.

Zhang, C., Huo, X., Zhu, Y., Higginbotham, J. N., Cao, Z., Lu, X., Franklin, J. L., Vickers, K. C., Coffey, R. J., Senapati, S., Wang, C., & Chang, H. C. (2022). Electrodeposited magnetic nanoporous membrane for high-yield and high-throughput immunocapture of extracellular vesicles and lipoproteins. *Communications Biology*, *5*(1), 1358.

Zhang, J., Nguyen, L. T. H., Hickey, R., Walters, N., Wang, X., Kwak, K. J., Lee, L. J., Palmer, A. F., & Reátegui, E. (2021). Immunomagnetic sequential ultrafiltration (iSUF) platform for enrichment and purification of extracellular vesicles from biofluids. *Scientific Reports*, *11*(1), 8034.

Zhang, L., Song, J., Cavigiolio, G., Ishida, B. Y., Zhang, S., Kane, J. P., Weisgraber, K. H., Oda, M. N., Rye, K. A., Pownall, H. J., & Ren, G. (2011). Morphology and structure of lipoproteins revealed by an optimized negative-staining protocol of electron microscopy. *Journal of Lipid Research*, *52*(1), 175–184.

Zhang, Y., Dube, C., Gibert, M. Jr, Cruickshanks, N., Wang, B., Coughlan, M., Yang, Y., Setiady, I., Deveau, C., Saoud, K., Grello, C., Oxford, M., Yuan, F., & Abounader, R. (2018). The p53 pathway in glioblastoma. *Cancers*, *10*(9), 297.

Zhou, J., Wu, Z., Hu, J., Yang, D., Chen, X., Wang, Q., Liu, J., Dou, M., Peng, W., Wu, Y., Wang, W., Xie, C., Wang, M., Song, Y., Zeng, H., & Bai, C. (2020). High-throughput single-EV liquid biopsy: Rapid, simultaneous, and multiplexed detection of nucleic acids, proteins, and their combinations. *Science Advances*, *6*(47), eabc1204.

Zottel, A., Šamec, N., Kump, A., Raspor Dall'Olio, L. R., Pužar Dominkuš, P., Romih, R., Hudoklin, S., Mlakar, J., Nikitin, D., Sorokin, M., Buzdin, A., Jovčevska, I., & Komel, R. (2020). Analysis of miR-9-5p, miR-124-3p, miR-21-5p, miR-138-5p, and miR-1-3p in glioblastoma cell lines and extracellular vesicles. *International Journal of Molecular Sciences*, *21*(22), 8491.

SUPPORTING INFORMATION

Additional supporting information can be found online in the Supporting Information section at the end of this article.

How to cite this article: Zhang, J., Rima, X. Y., Wang, X., Nguyen, L. T. H., Huntoon, K., Ma, Y., Palacio, P. L., Nguyen, K. T., Albert, K., Duong-Thi, M.-D., Walters, N., Kwak, K. J., Yoon, M. J., Li, H., Doon-Ralls, J., Hisey, C. L., Lee, D., Wang, Y., Ha, J., … Reátegui, E. (2023). Engineering a tunable micropattern-array assay to sort single extracellular vesicles and particles to detect RNA and protein in situ. *Journal of Extracellular Vesicles*, *12,* e12369. https://doi.org/10.1002/jev2.12369